Fluctuation and Stability in Potentiometric Sensors

Ngoc Anh Minh Tran

Department of Electrical & Computer Engineering

McGill University

Montréal, Québec, Canada

November 12, 2024

A thesis presented for the degree of Doctor of Philosophy

Abstract

This thesis concerns concepts in noise analysis, thermoelectric devices, and electrochemical sensors, presenting findings across these interconnected fields. In part one, the research advances the understanding of thermoelectric materials by extending the fluctuation-dissipation theorem to reveal the relationship between temperature and voltage fluctuations. This theoretical framework is validated through experiments with an ultra-fast thermoelectric micro-device, demonstrating an enhanced voltage fluctuation spectral density beyond the famed Johnson-Nyquist noise of Ohmic materials. The practical implications for temperature measurement by thermoelectric response are discussed.

In part two, $1/f$ noise in graphene field-effect transistors is studied, as this is the primary source of noise that limits the resolution of graphene field-effect transistor-based chemical sensors. Experiments demonstrating a facile method to reduce noise by scaling the active area of the sensors are presented, resulting in the lowest room temperature $1/f$ noise in a graphene transistor reported to date. This advancement leads to the development of

a sulfate ion sensor with unprecedented resolution of 1.2×10^{-3} log molar concentration units, showcasing the potential of graphene-based sensors in high-resolution chemical sensing applications.

Finally, in the third part, attention is turned to the reference electrode and its stability. All potentiometric sensors working in a liquid environment require an element sensitive to the analyte and a reference electrode. The study introduces a novel solid reservoir reference electrode designed to provide stable electrochemical measurements and overcome the high manufacturing cost, short shelf life, and wet storage requirements of traditional liquid-filled electrodes. The solid reservoir reference electrode features a construction analogous to the liquid-filled Ag/AgCl electrode, with an Ag/AgCl layer, a solid KCl reservoir, and a porous polydimethylsiloxane membrane, allowing for planar processing. The new electrode's performance is evaluated in aqueous and non-aqueous solvents like acetonitrile. The electrode's open circuit potential drift was less than 0.37 mV over 17 hours in deionized water and less than 3 mV over 8 hours in acetonitrile. In applications relating to electrocardiogram and electroencephalogram measurements, the solid reservoir reference electrode demonstrates a 50% improvement in signal-to-noise ratio.

Abrégé

Cette thèse porte sur des concepts d'analyse du bruit, de dispositifs thermoélectriques et de capteurs électrochimiques, et présente des résultats dans ces domaines interconnectés. Dans la première partie, la recherche fait progresser la compréhension des matériaux thermoélectriques en étendant le théorème de fluctuation-dissipation pour révéler la relation entre les fluctuations de température et de tension. Ce cadre théorique est validé par des expériences avec un micro-dispositif thermoélectrique ultra-rapide, démontrant une densité spectrale de fluctuation de tension améliorée au-delà du fameux bruit de Johnson-Nyquist des matériaux ohmiques. Les implications pratiques pour la mesure de la température par réponse thermoélectrique sont discutées.

Dans la deuxième partie, le bruit $1/f$ dans les transistors à effet de champ en graphène est étudié, car il s'agit de la principale source de bruit qui limite la résolution des capteurs chimiques basés sur des transistors à effet de champ en graphène. Des expériences démontrant une méthode facile pour réduire le bruit en augmentant la surface active des capteurs sont présentées, ce qui permet d'obtenir le plus faible bruit $1/f$ à température ambiante dans un

transistor au graphène rapporté à ce jour. Cette avancée conduit au développement d'un capteur d'ions sulfate avec une résolution sans précédent de $1,2\times10^{-3}$ unités de concentration molaire logarithmique, démontrant le potentiel des capteurs à base de graphène dans les applications de détection chimique à haute résolution.

Enfin, dans la troisième partie, l'attention se porte sur l'électrode de référence et sa stabilité. Tous les capteurs potentiométriques fonctionnant dans un environnement liquide nécessitent un élément sensible à l'analyte et une électrode de référence. L'étude présente une nouvelle électrode de référence à réservoir solide conçue pour fournir des mesures électrochimiques stables et surmonter les coûts de fabrication élevés, la courte durée de conservation et les exigences de stockage en milieu humide des électrodes traditionnelles remplies de liquide. L'électrode de référence à réservoir solide présente une construction analogue à l'électrode Ag/AgCl remplie de liquide, avec une couche Ag/AgCl, un réservoir KCl solide et une membrane poreuse en polydiméthylsiloxane, ce qui permet un traitement planaire. Les performances de la nouvelle électrode sont évaluées dans des solvants aqueux et non aqueux comme l'acétonitrile. La dérive du potentiel en circuit ouvert de l'électrode était inférieure à 0,37 mV pendant 17 heures dans l'eau désionisée et inférieure à 3 mV pendant 8 heures dans l'acétonitrile. Dans les applications relatives aux mesures de l'électrocardiogramme et de l'électroencéphalogramme, l'électrode de référence à réservoir solide améliore de 50 % le rapport signal/bruit.

Acknowledgements

First and foremost, I would like to thank my mother and father. Not only did they give me the gift of life, but they also provided unwavering support in my academic growth and personal development. Their constant encouragement to be the best version of myself has allowed me to reach where I am today.

I would like to thank my supervisor, Professor Thomas Szkopek. Not only has he been an amazing supervisor, but he has also been a great mentor, helping me navigate challenges beyond purely technical and academic matters. He has always encouraged me and all of his students to step back and think about the bigger picture of why we are doing what we do. He has consistently energized my curiosity, encouraging me to step out of my comfort zone and explore new topics unrelated to my PhD work. I could go on, but that would most likely make this thesis too long to read.

Without a doubt, the next person on the list is my academic sister, Melis Aygar. Like actual siblings, we don't always agree or get along, but despite our differences, Melis will always hold a special place in my heart for her help in getting my PhD on track. She has

taught me valuable microfabrication, characterization, and measurement techniques, which would have been extremely time-consuming and painful for me to learn on my own in a new environment. I also want to thank Yijin Xu for her support toward the end of my academic journey.

I would like to thank Oulin Yu and Zachary Marinov. Oulin introduced me to Thomas, and both have been invaluable friends, helping me through tough times. Christophe Clément is, without a doubt, the best microfabrication staff member I have ever worked with. Christophe has always gone above and beyond to help me and other students accomplish our projects, even calling in while on holiday to ensure things were running smoothly. Katya Marc and Derrick Wong at the McGill Engine have been more than helpful in assisting me with the transition out of my PhD and in kickstarting Ikei Systems. I would also like to thank Eli Martel and other lab members for the fun chats we had between experiments.

Contents

List of Figures

List of Acronyms

CSD	cross power spectral density.
CVD	chemical vapor deposition.
DNA	deoxyribonucelic acid.
DUT	device under test.
ECG	electrocardiogram.
EEG	electroencephalogram.
FET	field effect transistor.
GFET	graphene field-effect transistor.
ISE	ion-selective electrode.
ISFET	ion-sensetive field effect transistor.
MOSFET	metal–oxide–semiconductor field-effect transistor.
OCP	open circuit potential.
PDMS	polydimethylsiloxane.
PSD	power spectral density.

PVC	polyvinyl chloride.
RE	reference electrode.
REDOX	reduction-oxidation.
RIE	reactive ion etching.
SCE	saturated calomel electrode.
SHE	standard hydrogen electrode.
SNR	signal to noise ratio.
SRRE	solid reservoir reference electrode.
THF	tetrahydrofuran.

Chapter 1

Introduction

1.1 Overview

In this thesis, we aim to extend the understanding of measurement uncertainties and fluctuations in two technological areas of intense contemporary interest: thermoelectric sensors and graphene-based electrochemical sensors. While these two areas are seemingly disparate, both exhibit low-frequency noise with non-trivial behaviour that can be studied by similar experimental methods. In the course of my work investigating noise in graphene electrochemical sensors, the design of a stable reference electrode emerged as a topic of interest. For all electrochemical-based sensors, it is of utmost importance to have a true reference electrode to provide a stable potential of the analyte. Accordingly, in this thesis, we will discuss one of our inventions relating to reference electrodes, which we refer to as a

solid reservoir reference electrode. Let us first give a very brief introduction to thermoelectricity, voltage fluctuations in resistors, and the development of graphene.

Thermoelectric materials have been useful to our society ever since the first thermoelectric generator was developed to power a radio from an oil-burning lamp in 1948 [1]. The first thermoelectric effect was observed in 1821 by Thomas Johann Seebeck [2]. He observed the deflection of a compass needle close to two metal junctions which were kept at different temperatures. Quantitatively, we define the Seebeck coefficient of a material S to be the ratio between the voltage difference across a material ΔV and the temperature difference ΔT:

$$S = -\frac{\Delta V}{\Delta T}, \tag{1.1}$$

where the material has come to a steady state, with all current densities being zero [3]. In 1834, a watchmaker and part-time physicist Jean C.A. Peltier found that an electric current could produce heating or cooling at the junction of two similar metals [4]. This effect is quantitatively described as follows. Let A and B be two conductors, the heat flow from A to B per unit time is given as:

$$\frac{\mathrm{d}Q}{\mathrm{d}t} = (\Pi_A - \Pi_B)I, \tag{1.2}$$

where Π_A and Π_B are the Peltier coefficients of conductors A and B respectively, with I being

the electric current. Exactly 20 years later, William Thomson issued an elegant explanation of the observations from Seebeck and Peltier through thermodynamic relations [5]. The Seebeck coefficient is related to the Peltier coefficient by the exact relation

$$S = \frac{\Pi}{T}, \tag{1.3}$$

where T is the average temperature of the material. The observations by Thomson, Peltier, and Seebeck formed the basis for our understanding of thermoelectricity.

Most modern thermoelectric research primarily focuses on discovering and optimizing new materials that can efficiently convert heat into electricity, not only for thermoelectric generators but also to advance state-of-the-art thermoelectric-based infrared imaging [6] and enable temperature measurements at the single-cell level [7]. This research involves exploring materials with high thermoelectric efficiency, characterized by a high Seebeck coefficient, low thermal conductivity, and high electrical conductivity. Researchers are continuously investigating novel compounds, nanostructured materials, and innovative fabrication techniques to enhance these properties [8–11]. However, a critical aspect that has been largely overlooked in this field is the fundamental noise in thermoelectric materials. This intrinsic noise, arising from temperature and voltage fluctuations, can significantly impact the performance and reliability of thermoelectric devices. Yet, it has not been thoroughly addressed or studied in the context of improving thermoelectric

materials and technologies.

Let us now give a brief history of voltage fluctuations in resistors. In 1926, John B. Johnson, who was working in the physics division at Bell Labs, was researching noise in electronic circuits. He observed that there was an irreducible low level of noise in resistors and that its power was proportional to the temperature. Johnson described his findings to Harry Nyquist, who then arrived at the first theory of Johnson noise [12]. The voltage power spectral density, or voltage variance per unit bandwidth, is given by

$$S_V(f) = 4k_BTR, \tag{1.4}$$

where k_B, T, and R are the Boltzmann constant, the average temperature, and the electrical resistance, respectively. In 1951, Herbert Callen and Theodore Welton demonstrated how Johnson noise could be explained through the more general fluctuation-dissipation theorem [13]. This theorem describes how thermodynamic fluctuations in a physical variable are determined by the impedance of that same variable and vice versa. Contemporary research on noise in conductors focuses on understanding and modeling noise under extreme conditions, at high frequencies and low temperatures, where $\hbar\omega > k_BT$ [14, 15]. Here, $\hbar$ and ω represent the reduced Planck's constant and angular frequency, respectively. Although both the theories of thermoelectricity and fluctuation-dissipation have been well established for nearly 100 years, there has yet to be a

theory that unifies the two. In this work, it will be shown that the low-frequency Johnson noise of a thermoelectric material is modified by its thermoelectric response.

Turning our attention to the other material system that is studied in this thesis, we give a very brief introductory synopsis of graphene. The story of graphene started in 1859, when the English chemist Sir Benjamin Collins Brodie observed the highly layered structure of thermally reduced graphite oxide. It took another 88 years, in 1947, for Phillip Russel Wallace at the National Research Council of Canada to consider the theoretical existence of graphene [16]. Efforts to make graphene through mechanical exfoliation started in 1990, but nothing thinner than 50 layers was produced [17]. In 2004, Andre Geim and Konstantin Novoselov used adhesive tape to pull graphene layers from graphite and transfer them onto SiO_2/Si wafers [18]. The voltage modulation of the silicon beneath the SiO_2 allows for the charge carrier density of the graphene to be modulated, creating the first field-effect transistor (FET) with a material that has no bandgap. In 2009, Luigi Colombo and Rodney Ruoff showed how large-area monolayer graphene can be synthesized through chemical vapor deposition on Cu [19]. The discoveries by Colombo, Ruoff, Geim, and Novoselov kickstarted research and development in graphene-based sensors, where we have seen applications in electrochemical sensors [20], strain sensors [21], and magnetic field sensors [22]. A significant impediment in all graphene-based sensors is low-frequency $1/f$ noise. It is observed that the $1/f$ noise in graphene FETs is influenced by several factors, including the quality of the graphene material, the presence of impurities, and the nature of the substrate on which the

graphene is placed [23–25]. Research continues to focus on understanding the underlying mechanisms of $1/f$ noise in graphene FETs [26, 27]. Understanding the physical phenomena and parameters, which dictate $1/f$ noise in graphene, will allow for the diminishment of $1/f$ noise and bring graphene sensors closer to serving our society.

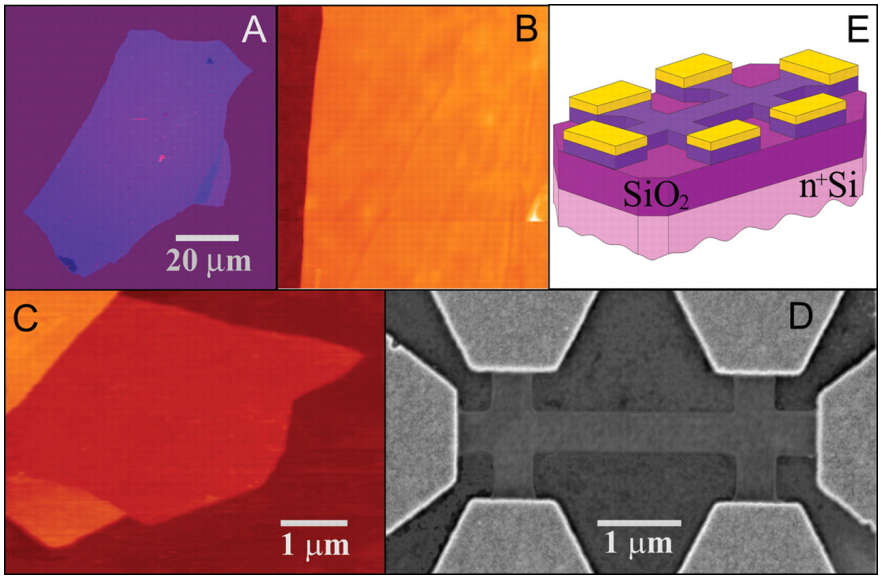

Figure 1.1: Graphene films. (A) Photograph (in normal white light) of a relatively large multilayer graphene flake with thickness approximately 3 nm on top of an oxidized Si wafer. (B) Atomic force microscope (AFM) image of 2 μm by 2 μm area of this flake near its edge. Colors: dark brown, SiO_2 surface; orange, 3 nm height above the SiO_2 surface. (C) AFM image of single-layer graphene. Colors: dark brown, SiO_2 surface; brown-red (central area), 0.8 nm height; yellow-brown (bottom left), 1.2 nm; orange (top left), 2.5 nm. Notice the folded part of the film near the bottom, which exhibits a differential height of $\sim$0.4 nm. For details of AFM imaging of single-layer graphene, see [18]. (D) Scanning electron microscope image of one of our experimental devices prepared from FLG. (E) Schematic view of the device in (D). [18]

1.2 Original Contributions

In this thesis, the following original contributions are reported.

- **Extension of the fluctuation-dissipation theorem to thermoelectric systems.** The coupling between temperature fluctuations and voltage fluctuations, along with the effect on electrical and thermal impedance, was theoretically demonstrated in thermoelectric materials and modules.

- **Experimental measurement of temperature fluctuations with an amplitude of 0.8 μK Hz^{-1} in an ultra-fast thermoelectric module.** Temperature fluctuations were measured in ultra-fast thermoelectric modules by observing voltage fluctuations and understanding the coupling between voltage and temperature fluctuations. By correlating these fluctuations with the electrical impedance of the device, the fluctuation-dissipation theorem was experimentally extended to thermoelectric materials and modules.

- **Experimental measurement of 1/f noise in graphane field effect transistors and graphene ion selective field effect transistor, demonstrating a facile method to reduce 1/f noise in graphene.** 1/f noise of various graphene field effect transistor was fabricated and measured, demonstrating that the noise power is inversely dependent of the active device area, allowing for the fabrication of an ultra-low noise and ultra-high resolution sulfate sensors.

- **Invention and quantification of the improved performance of a compact and low-cost reference electrode.** A new reference electrode compatible with planar processing was developed. This novel electrode demonstrated superior performance for compact electrochemical sensors in both aqueous and non-aqueous environments. The electrode's open-circuit potential drift was less than 0.37 mV over 17 hours in deionized water and less than 3 mV over 8 hours in acetonitrile. The open-circuit potential variation of the electrode was less than 1 mV across two orders of magnitude variation in chloride ion concentration. In bio-signal measurement applications, the new electrode achieved a 50% improvement in signal-to-noise ratio for electrocardiogram and electroencephalogram measurements.

The work presented in this thesis resulted in the following selected list of publications and conference talks, with the contributions explicitly listed.

1. Tran NA, Fakih I, Durnan O, Hu A, Aygar AM, Napal I, Centeno A, Zurutuza A, Reulet B, Szkopek T. Graphene field effect transistor scaling for ultra-low-noise sensors. Nanotechnology. 2020 Nov 5;32(4):045502.

    - This work was conceived by N. Tran and T. Szkopek. N. Tran and T. Szkopek prepared the manuscript with contributions from all co-authors.
    - N. Tran fabricated the scaled van der Pauw structures with technical assistance from A. Aygar.

- N. Tran performed all the noise measurements with assistance from A. Hu and B. Reulet.
- The Hall measurements were performed by O. Durnan.
- I. Napal, A. Centeno and A. Zurutuza grew and transferred wafer scale graphene.
- I. Fakih fabricated and characterized graphene ISFET structures.

2. Tran NA, Dutt AS, Pulumati NB, Reith H, Hu A, Dumont A, Nielsch K, Tremblay AMS, Schierning G, Reulet B, Szkopek T. Fluctuation-dissipation in thermoelectric sensors. Europhysics Letters. 2023 Jan 19;141(2):26002.

- This work was conceived by N. Tran, B. Reulet and T. Szkopek. N. Tran, B. Reulet and T. Szkopek prepared the manuscript with contributions from all co-authors.
- Noise measurements were carried out by N. Tran with the help of A. Dumont, T. Szkopek, and B. Reulet.
- Impedance measurements were carried out by N. Tran.
- Data analysis was carried out by N. Tran with the help of A. Hu.
- Quantum field analysis was carried out by A.M.S. Tremblay.
- The ultra-fast thermoelectric device was fabricated by A. Dutt, N. Pulumati, H. Reith, G. Schierning and K. Nielsch.

3. Tran MN, Capilli G, Szkopek T. Solid Reservoir Reference Electrode. InElectrochemical Society Meeting Abstracts 244 2023 Dec 22 (No. 63, pp. 3019-3019). The Electrochemical Society, Inc..

    - This work was conceived by N. Tran and T. Szkopek.
    - All device fabrication was performed by N. Tran with the help of G. Capilli.
    - All measurements were performed by N. Tran with the help of G. Capilli.
    - All data analysis was performed by N. Tran.

1.3 Thesis Outline

The structure of this thesis is as follows.

Chapter 2: This chapter introduces key concepts of power spectral density with clear and precise mathematical definitions. It covers the derivation of essential noise formulas, such as Johnson-Nyquist noise and 1/f noise originating from charge trap states. The discussion also extends to cross-spectral density and the use of the cross-periodogram method for precise cross-spectral density estimation. Additionally, the chapter includes detailed circuit noise models relevant to voltage amplifiers. It explores voltage cross-correlation measurements as a strategic method for evaluating device noise, especially when the spectral density of the device noise is lower than that of the amplifier noise.

Chapter 3. This chapter introduces essential electrochemistry concepts for the

subsequent chapters. It starts with the role of reference electrodes in electrochemical measurements, then explores three types of reference electrodes: the standard hydrogen electrode, the saturated calomel electrode, and the silver chloride reference electrode. Finally, it discusses the principles of traditional ion-selective electrodes and ion-sensitive field-effect transistors.

Chapter 4. This chapter is a reproduction of the published work relating to the extension of the fluctuation-dissipation theorem on thermoelecric materials. This work theoretically demonstrates the coupling between temperature fluctuations and voltage fluctuations of ohmic origins, revealing an enhanced voltage fluctuation spectral density $4k_BTR(1 + ZT)$ below a thermal cut-off frequency f_T, where ZT is the dimensionless thermoelectric figure of merit. Experimental measurements were conducted on an ultra-fast($f_T \sim 1$ kHz) integrated thermoelectric micro-device, confirming the theoretical predictions. The ZT-enhanced voltage noise enabled the resolution of temperature fluctuations with an amplitude of 0.8 μK Hz$^{-1/2}$ at 295 K.

Chapter 5. This chapter is a reproduction of the published work on 1/f noise in graphene field effect transistors and ion-selective field effect transistors. A straightforward technique is presented to reduce $1/f$ noise by scaling the active area of graphene field effect transistor sensors. Measurements of $1/f$ noise in graphene field effect transistors with sizes ranging from 5 μm$\times$5 μm to 5.12 mm$\times$5.12 mm achieved a reduction in $1/f$ noise by more than five orders of magnitude. This resulted in the lowest normalized graphene $1/f$ noise parameter recorded

to date, 5×10^{-13}. Additionally, a sulfate ion sensor with an unprecedented resolution of 1.2×10^{-3} log molar concentration units was developed.

Chapter 6. This chapter reproduces a manuscript in preparation for submission on the invention and performance characterization of a compact and cost-effective reference electrode. A novel reference electrode, the solid reservoir reference electrode, is introduced to replace traditional liquid-filled Ag/AgCl electrodes. The solid reservoir reference electrode features a Ag/AgCl paint layer, a solid KCl reservoir, and a porous polydimethylsiloxane membrane. Its performance was evaluated in both aqueous and non-aqueous solvents, including acetonitrile. The chapter also assesses the performance of a dual ion sensor by integrating the solid reservoir reference electrode (SRRE) with a graphene ion-sensitive field-effect transistor sensitive to pH and Na^+ ions. Additionally, the SRRE's signal quality in bioelectrode applications was evaluated, demonstrating improved electrocardiogram and electroencephalogram recordings.

Chapter 7. This chapter provides a summary and synthesis of the main findings and outcomes of the research and development. It present suggestions on potential future research and developement work.

Chapter 2

Review of Noise in Electrical Devices

In electrical systems, noise is typically an unwanted disturbance. Noise can be divided into two categories: interference noise and fundamental noise. Noise from external influences outside the system is called interference noise, with examples being temperature drifts which induce a drift in the electronics amplification, mechanical vibrations which can modulate capacitance and induce unwanted voltages, and lastly, electromagnetic fields interference originating from other electronic devices. While interference noise can be mitigated through the isolation of the system, fundamental noise cannot, as it is inherent to the system itself. Examples of fundamental noises are 1/f noise, shot noise and Johnson noise.

This review will prepare the reader for understanding the way noise is quantitatively described, measured and analyzed in subsequent chapters of this work. In this Chapter, we start by introducing the mathematical definitions of the power spectral density (PSD). We

proceed to derive the well-known Johnson-Nyquist noise formula, and the PSD of 1/f noise induced through charge trap states. Subsequently, we define the cross-spectral density (CSD) and the cross-periodogram method to estimate the CSD. We follow with the discussion of the circuit noise model associated with voltage amplifiers. Finally, we describe voltage cross correlation measurement as a means to measure device noise whose power spectral density is below that of available amplifier noise spectral density.

2.1 Power spectral density

The PSD is often used to quantitatively characterize noise. We will thus describe the mathematical definitions for the PSD. Let $V(t)$ be the voltage noise as a function of time. We define its autocorrelation to be

$$R_{VV}(\tau) = \lim_{X\to\infty} \frac{1}{X} \int_{-X/2}^{X/2} V(t+\tau)V(t)dt. \tag{2.1}$$

From the Wiener–Khinchin theorem, the PSD of the function is the Fourier transform of the function's autocorrelation function

$$S_V(f) = \int_{-\infty}^{\infty} R_{VV}(\tau)e^{-2\pi i f\tau}d\tau. \tag{2.2}$$

If the expectation value of $V(t)$ is zero, i.e.

$$E(V(t)) = \lim_{X\to\infty} \frac{1}{X} \int_{-X/2}^{X/2} V(t)dt = 0, \tag{2.3}$$

the power of $v_1(t)$ is also its variance and can be computed through the summation of the PSD, i.e.

$$P_V = var(V(t)) = \lim_{X\to\infty} \frac{1}{X} \int_{-X/2}^{X/2} V(t)^2 dt = \int_{-\infty}^{\infty} S_V df \tag{2.4}$$

White noise processes like Johnson noise and shot noise have a constant PSD, which is independent of frequency over the bandwidth of interest (Fig. 2.1a). Flicker noise processes have a PSD that is inversely proportional to frequency, $S_{V_f} = A/f$, where A is the proportionality constant and f the frequency. If the flicker noise was plotted on a log-log scale, a straight line with a downward slope of -1, as would be seen in Fig. 2.1b.

2.2 Review of Johnson-Nyquist noise

If all sources of electrical power are removed from a resistor, from Ohm's law, one would expect the measured voltage to be precisely zero. In reality, there are voltage fluctuations across the resistor with mean squared valued proportional to absolute temperature. Fluctuations of thermal origin was first described by Albert Einstein in 1905, to explain

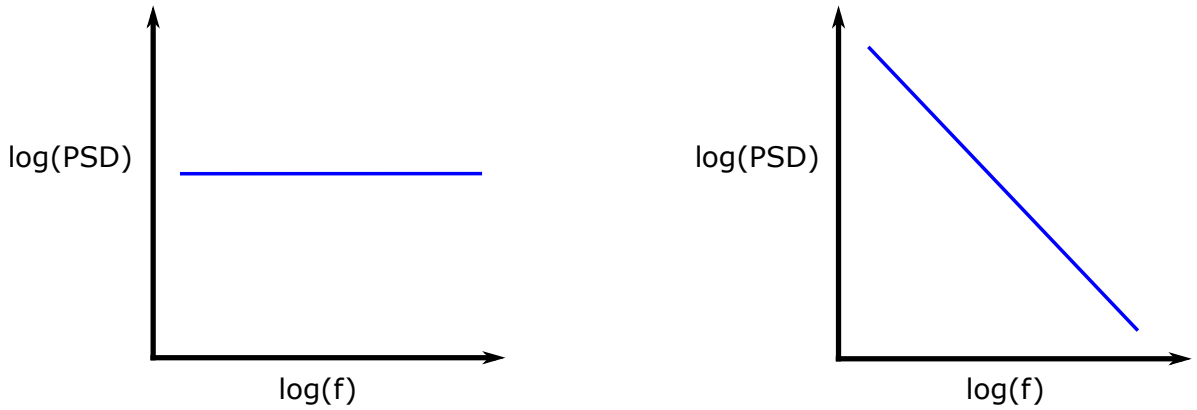

(a) **(b)**

Figure 2.1: (a) Representative schematic of a white noise process, where the PSD is constant and is independent of frequency over the bandwidth of interest. (b) Representative schematic of a 1/f noise process, where the PSD is inversely proportional to frequency, with a slope of -1 on a log-log plot.

Brownian motion [28]. Johnson was the first to observe fluctuations of thermal origin in resistors, now commonly referred to as Johnson noise [12]. The findings paved the way for Callen, Welton and Kubo to unify the theory of Brownian motion and Johnson noise through the fluctuation-dissipation theorem [13, 29].

We reproduce here the derivation of Johnson-Nyquist noise using transmission line theory. We consider a lossless transmission line of length L terminated at both ends with resistor R_1 and R_2, as can be seen in Fig. 2.2. The characteristic impedance of the transmission line Z, the resistance of R_1 and R_2 are all identically R. As such, any voltage wave propagating along the transmission line is completely absorbed at both ends, as all the impedances are

matched in the system. Voltage wave propagating down the transmission line takes the form

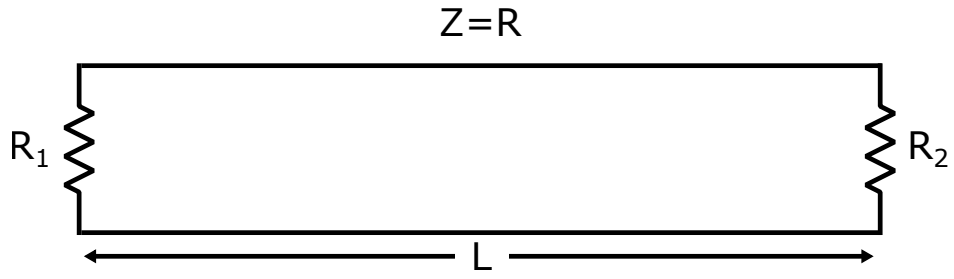

Figure 2.2: Lossless transmission line model with characteristic impedance $Z = R$, terminating resistances $R_1 = R_2 = R$ and length L.

$V = V_0 e^{i(k_x x - 2\pi f t)}$, at velocity $v = 2\pi f/k_x$. As the transmission line is perfectly matched and symmetric, the waves must satisfy the periodic boundary condition $V(0) = V(L)$. After imposing the boundary condition, we find that the k_x can only take on discrete values, where $k_x = 2\pi n/L$, with n being any integer. The density of modes per unit length and unit frequency is then,

$$D(f) = \frac{\mathrm{d}n}{\mathrm{d}f} = \frac{\mathrm{d}n}{\mathrm{d}k_x}\frac{\mathrm{d}k_x}{\mathrm{d}f} = \frac{L}{v}. \tag{2.5}$$

The mean energy per mode is given by Planck formula,

$$\langle \epsilon(f) \rangle = \frac{2\pi z \hbar f}{e^{2\pi\hbar f/(k_B T)} - 1}, \tag{2.6}$$

in the classical limit where $2\pi\hbar f \ll k_B T$, and taking the first order approximation of the exponential, we get the approximate mean energy per mode to be

$$\langle \epsilon(f) \rangle \approx k_B T. \tag{2.7}$$

The energy density per unit frequency $U(f)$ is given by the product of the density of modes and the mean energy per mode,

$$U(f) = D(f)\langle \epsilon(f) \rangle = \frac{k_B T L}{v}. \tag{2.8}$$

Given that L/v is the propagation time, Δt, then the power per unit frequency is,

$$P(f) = \frac{U(f)}{\Delta t} = k_B T. \tag{2.9}$$

By the principle of detailed balance, the power per unit frequency absorbed by the resistor must also be the power emitted by the resistor at thermal equilibrium. In our transmission line system, as the resistors are perfectly matched, with identical resistance, the electrical current through the system is $I = V/(2R)$. Thus the power absorbed by one resistor per unit frequency is

$$P(f) = \langle I^2(f) \rangle R = \frac{\langle V^2(f) \rangle}{4R}. \tag{2.10}$$

Equating Eq. (2.9) with Eq. (2.10), and solving for the mean-square voltage per unit frequency and voltage power spectral density we get,

$$\langle V^2(f)\rangle = S_V(f) = 4k_BTR \tag{2.11}$$

Integrating over all frequencies, we get the variance of voltage fluctuations and the well established Johnson-Nyquist noise formula,

$$\langle V^2\rangle = \int_0^{\Delta f} 4k_BTR \, \mathrm{d}f = 4k_BTR\Delta f. \tag{2.12}$$

This understanding of Johnson-Nyquist noise has allowed us to set a fundamental limit on measurement accuracy and resolution in many electrical sensors and devices. Although the theory of thermoelectricity, fluctuation-dissipation and temperature fluctuations have been well established for more than 4 decades [4, 29, 30], the coupling between temperature fluctuations and voltage fluctuations has not been demonstrated experimentally. Chapter 4 of this thesis contains the article published in Europhysics Letter in relation to this work [31].

2.3 Review of 1/f noise

Flicker noise or 1/f noise was first observed in 1925 [32], when John B. Johnson was performing noise measurement in vacuum tubes, designed to test Schottky's theory of shot

noise. Johnson noticed that at low frequencies the power spectral density, instead of remaining constant, was inversely proportional to frequency. 1/f noise was later observed in a vast array of systems, ranging from metal oxide semiconductors [33] and economics [34] to human cognition [35]. In all resistive devices, 1/f noise can originate from either fluctuations in charge carrier number N_C, charge carrier mobility μ_C, or a combination of the two. For vacuum tubes and graphene field effect transistors, it is believed that 1/f noise is dominated by fluctuations in number of charge carriers due to the large abundance of charge-traps in the system [36]. As such, we will give the derivation for 1/f noise of contributions from charge carrier fluctuations.

If a free carrier in a conducting channel is immobilized due to a charge trap, it no longer contributes to the electrical conductance of the material. Let $x(t)$ be the normalized modulation of charge carrier numbers due to a single charge trap. It has the form of a random telegraph signal with a Poisson point process, which is a suitable description for charge traps that are invariant in time. $x(t)$ can take on the value of +1 in the free state and -1 in the trapped state (Fig. 2.3). The probability of observing m transitions of the charge trap, either trapping or freeing a charge carrier, in a time interval T is given by:

$$p(m,T) = \frac{(\nu T)^m}{m!} e^{-\nu T}, \tag{2.13}$$

where ν is the mean rate of transitions per second. Let τ_t and τ_f be the average times

the charge trap spends in the trapping and freeing states, respectively. The probability distributions of the trapped state time t_t and free state time t_f before a transition occurs are given by

$$p(t_t) = \frac{1}{\tau_t} e^{-\frac{t_t}{\tau_t}}, \tag{2.14}$$

$$p(t_f) = \frac{1}{\tau_f} e^{-\frac{t_f}{\tau_f}}. \tag{2.15}$$

If an even number of transitions occurred in the interval $(t, t+\tau)$, then $x(t)x(t+\tau) = 1$,

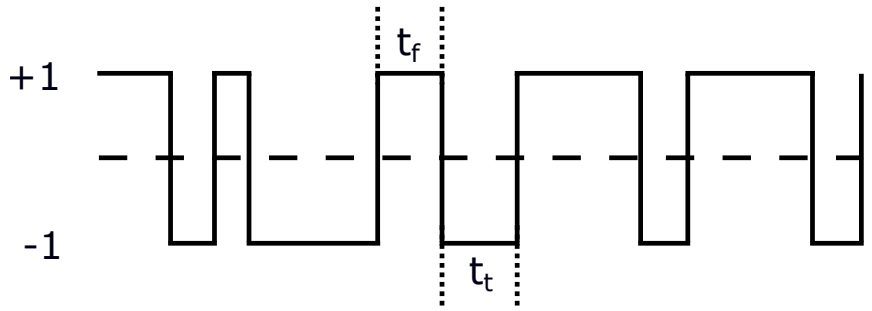

Figure 2.3: Representative schematic of a random telegraph signal caused by a single charge trap.

while if an odd number of transitions occurred in the same interval, $x(t)x(t+\tau) = -1$. The

autocorrelation of this signal is therefore

$$\begin{aligned}\phi_x(\tau) &= [p(0,\tau) + p(2,\tau) + \ldots] - [p(1,\tau) + p(3,\tau) + \ldots] \\ &= e^{-\nu|\tau|}\left[1 - \nu|\tau| + \frac{(\nu|\tau|)^2}{2!} - \frac{(\nu|\tau|)^3}{3!} + \ldots\right] \\ &= e^{-2\nu|\tau|}.\end{aligned} \tag{2.16}$$

From the Wiener-Khintchine theorem, the power spectral density is just the Fourier transform of the autocorrelation function. Therefore, the power spectral density from a single charge trap is

$$\begin{aligned}S_x(f) &= \int_{-\infty}^{\infty} \phi_x(\tau) e^{i2\pi f\tau} d\tau = \frac{1/\nu}{1 + (2\pi f)^2/(4\nu^2)} \\ &= \frac{2\tau_x}{1 + (2\pi f \tau_x)^2}.\end{aligned} \tag{2.17}$$

where $\tau_x = 1/(2\nu)$ is the time constant of the charge trap. Note that the PSD has the form of a Lorentzian. From the charge carrier tunneling model [37], the trapping of charges due to the tunneling of charge carriers from a conducting layer to trap sites inside the oxide layer of depth w will have a time constant given by

$$\tau_x = \tau_0 e^{\gamma w}, \tag{2.18}$$

where τ_0 and γ are constants. If the traps are uniformly distributed and only present between depths w_1 and w_2, corresponding to the trap time constants τ_1 and τ_2, the probability

distribution as a function of the trap's time constant is

$$p(\tau_x) = \begin{cases} \frac{\ln(\tau_1/\tau_2)}{\tau_x} & \text{for } \tau_1 \leq \tau_x \leq \tau_2 \\ 0 & \text{elsewhere} \end{cases} \tag{2.19}$$

The power spectral density of charge carrier fluctuations due to all the charge trap states is

$$\begin{aligned} S(f) &= \int_0^\infty S_x(f) p(\tau_x) d\tau_x \\ &= 2\ln(\tau_1/\tau_2) \int_{\tau_1}^{\tau_2} \frac{d\tau_x}{1 + (2\pi f \tau_x)^2} \\ &= 2\ln(\tau_1/\tau_2) \frac{[\tan^{-1}(2\pi f \tau_2) - \tan^{-1}(2\pi f \tau_1)]}{2\pi f} \\ &\approx \begin{cases} 2\ln(\tau_1/\tau_2)(\tau_2 - \tau_1), & \text{for } 0 \ll f \ll 1/(2\pi\tau_2) \\ \frac{\ln(\tau_1/\tau_2)}{2f} & \text{for } 1/(2\pi\tau_2) \ll f \ll 1/(2\pi\tau_1) \\ \frac{2\ln(\tau_1/\tau_2)(\tau_2 - \tau_1)}{\tau_2 \tau_1 (2\pi)^2} \frac{1}{f^2} & \text{for } 1/(2\pi\tau_1) \ll f. \end{cases} \end{aligned} \tag{2.20}$$

At very low frequencies, below the cut-off $1/(2\pi\tau_2)$, all traps contribute a flat spectral density. At intermediate frequencies, the contribution from the full distribution of fluctuating traps, with some in the flat regime and some in high frequency $1/f^2$ regime, contributing to an overall 1/f PSD. At high frequency, above the cut-off for the fastest trap, all of traps contribute to give effectively a $1/f^2$ to the PSD. In practice, the 1/f regime is most commonly observed, as measuring the voltage noise in the low-frequency

range requires long measurement time, while at high frequencies, other noise sources like shot noise or Johnson noise dominate.

Regardless of whether 1/f fluctuations originate from carrier mobility or from charge-trap states, all types of 1/f noise in conductors, semiconductors, and other electronic materials can be characterized by their power spectral density,

$$\frac{S_V(f)}{V^2} = \frac{S_I(f)}{I^2} = \frac{S_R(f)}{R^2} = \frac{\alpha_H}{N_C f}, \tag{2.21}$$

where $S_V(f)$, V, $S_I(f)$, I, $S_R(f)$, R, α_H, N_C, and f are the voltage power spectral density, voltage, current power spectral density, current, resistance power spectral density, resistance, Hooge parameter, number of charge carriers, and frequency, respectively. The power spectral densities being inversely proportional to the total number of charge carriers N_C can be intuitively understood as follows: regardless of the mechanism that causes the electrons or holes to produce the 1/f spectrum, they do so independently of each other. Thus, from the law of large numbers, the total power of their fluctuations (variance) and power spectral density must be inversely proportional to the total number of holes or electrons in the system. Chapter 5 of this thesis contains the article that was published in *Nanotechnology* [38], where 1/f noise scaling with physical device area was studied in FETs.

2.4 Cross-spectral density

The cross power spectral density (CSD), is a powerful signal processing tool. It is employed when the noise power PSD of the device under test (DUT) is smaller than the PSD of the available amplifiers. In anticipation of experimental measurements of a noise source $V(t)$ with two amplifiers that themselves contribute local noise voltage sources $e_1(t)$ and $e_2(t)$, we consider $v_1(t)$ and $v_2(t)$ as two voltages measured by amplifiers 1 and 2, where

$$v_1(t) = V(t) + e_1(t), \tag{2.22}$$

$$v_2(t) = V(t) + e_2(t). \tag{2.23}$$

We assume that $V(t)$, $e_1(t)$ and $e_2(t)$ are uncorrelated and that each has a zero expectation value, we thus find the cross-spectral density between $v_1(t)$ and $v_2(t)$ to be

$$\begin{aligned} R_{v_1v_2}(\tau) &= \lim_{X\to\infty}\frac{1}{X}\int_{-X/2}^{X/2} v_1(t+\tau)v_2(t)dt. \\ &= \lim_{X\to\infty}\frac{1}{X}\int_{-X/2}^{X/2}[V(t+\tau)+e_1(t+\tau)][V(t)+e_2(t)]dt \\ &= \lim_{X\to\infty}\frac{1}{X}\int_{-X/2}^{X/2} V(t+\tau)V(t)dt + \lim_{X\to\infty}\frac{1}{X}\int_{-X/2}^{X/2} e_1(t+\tau)V(t)dt + \\ &\quad \lim_{X\to\infty}\frac{1}{X}\int_{-X/2}^{X/2} V(t+\tau)e_2(t)dt + \lim_{X\to\infty}\frac{1}{X}\int_{-X/2}^{X/2} e_1(t+\tau)e_2(t)dt \\ &= R_{VV}(\tau) + 0R_{e_1V}(\tau) + 0R_{Ve_2}(\tau) + 0R_{e_1e_2}(\tau). \\ &= R_{VV}(\tau) \end{aligned} \tag{2.24}$$

The CSD of $v_1(t)$ and $v_2(t)$ is thus

$$\begin{aligned} S_{v_1v_2}(f) &= \int_{-\infty}^{\infty} R_{v_1v_2}(\tau)e^{-2\pi i f\tau}d\tau \\ &= \int_{-\infty}^{\infty} R_{VV}(\tau)e^{-2\pi i f\tau}d\tau \\ &= S_V(f) \end{aligned} \tag{2.25}$$

We can therefore see how the CSD is a useful tool to extract the correlated voltage.

Estimating the cross spectral density of sampled data

In practice, to estimate $S_{v_1v_2}(f)$ and $S_V(f)$, the cross-periodogram approximation method is often used [39]. The cross-periodogram method reduces to the periodogram method when it is applied to a single time series of voltages. The cross-periodogram method entails that, the signals $v_1(t)$ and $v_2(t)$ are periodically and simultaneously sampled with sampling period Δt. The acquired samples of the two sets of data is denoted by $v_1[n]$ and $v_2[n]$, $n = 1, 2, \ldots$. We acquire NM samples split into M groups of N samples, the cross-periodogram associated to group $m = 1, ..., M$, is

$$\tilde{S}_{v_1v_2,m}(f_k) = \frac{(\Delta t)}{N}\overline{\left[\sum_{n=1}^{N} v_1[(m-1)N+n]e^{-2\pi i f_k n\Delta t}\right]}\left[\sum_{n=1}^{N} v_2[(m-1)N+n]e^{-2\pi i f_k n\Delta t}\right], \tag{2.26}$$

where $f_k = k/(N\Delta t)$, $k = 0, ..., N-1$, are the Fourier frequencies and the overline denotes complex conjugation. The frequency resolution is $1/(N\Delta t)$. The average of the M periodograms,

$$\tilde{S}_{v_1v_2}(f_k) = \frac{1}{M}\sum_{m=1}^{M}\tilde{S}_{v_1v_2,m}(f_k), \tag{2.27}$$

is the estimator of $S_{v_1v_2}(f_k)$. In the limit of large M, the estimator approaches the CSD at the frequencies, f_k for large values of M.

$$\lim_{M\to\infty}\frac{1}{M}\sum_{m=1}^{M}\tilde{S}_{v_1v_2,m}(f_k) = S_{v_1v_2}(f_k), \tag{2.28}$$

The variance of the M periodograms can be shown [39] for large enough M to be well approximated by

$$var(\tilde{S}_{v_1v_2,m}(f_k)) = \left[\frac{1}{M}\sum_{m=1}^{M}[\tilde{S}_{v_1v_2,m}(f_k)^2]\right] - \left[\frac{1}{M}\sum_{m=1}^{M}[\tilde{S}_{v_1v_2,m}(f_k)]\right]^2 \sim S_{v_1}(f_k)S_{v_2}(f_k). \tag{2.29}$$

From the law of large numbers, as $\tilde{S}_{v_1v_2}(f_k)$ is the average of the M periodograms, the variance of the estimator is

$$var(\tilde{S}_{v_1v_2}(f_k)) = \lim_{I\to\infty}\left[\left[\frac{1}{I}\sum_{i=1}^{I}[\tilde{S}_{v_1v_2,i}(f_k)^2]\right] - \left[\frac{1}{I}\sum_{i=1}^{I}[\tilde{S}_{v_1v_2,i}(f_k)]\right]^2\right] \sim \frac{1}{M}S_{v_1}(f_k)S_{v_2}(f_k), \tag{2.30}$$

where $\tilde{S}_{v_1v_2,i}(f_k)$ is the i-th measurement of $\tilde{S}_{v_1v_2}(f_k)$.

2.5 Measuring voltage power spectral density

We will be using the noise model in Fig. 2.4 for the noise analysis of voltage amplifiers in all of my thesis work. We use the universal linear amplifier noise model, as presented in Chapter 9.3 of *Analog Integrated Circuit Design* [40], where a noiseless amplifier with gain A and input impedance Z_{in} has an equivalent voltage noise source $e_{n1}(t)$ and an equivalent current noise source $i_{n1}(t)$ (Fig. 2.4). The output voltage of the amplifier, with a short-circuited input is exactly $Ae_{n1}(t)$. The output voltage of the amplifier with an open-circuited input is exactly $AZ_{in}i_{n1}(t)$. Therefore, $e_{n1}(t)$ can be experimentally measured by applying a short circuit to the input of the amplifier, while $i_{n1}(t)$ can be experimentally measured by applying an open circuit to the input of the amplifier.

2.5.1 Direct measurement of the PSD

When the noise contributions from the amplifier are negligible compared to that of the device under test (DUT), a direct measurement as shown in Fig. 2.5 is sufficient to measure the DUT's PSD. In this subsection we will analyze the quantitative conditions to warrant a direct PSD measurement. The voltage at the input of the noiseless amplifier $v_1(t)$ in a direct

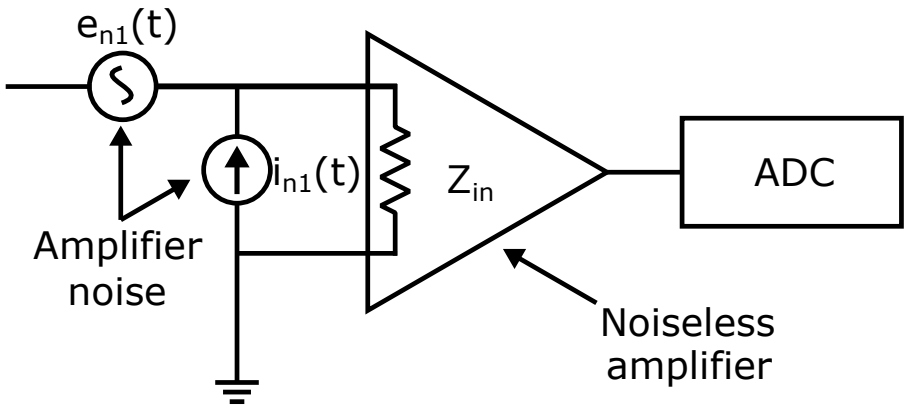

Figure 2.4: Noise circuit model for voltage amplifiers; $e_{n1}(t)$, $i_{n1}(t)$, and Z_{in} are the equivalent voltage noise, current noise, and impedance respectively. ADC is the analog to digital converter.

measurement as shown in Fig. 2.5 is

$$v_1(t) = \frac{Z_{in}}{Z_{in}+R}\Big(e_{n1}(t)+V(t)\Big) + \frac{Z_{in}R}{Z_{in}+R}i_{n1}(t) \tag{2.31}$$

If the input impedance of the amplifier is large enough such that $Z_{in} >> R$, it follows that

$$v_1(t) \approx e_{n1}(t) + V(t) + i_{n1}(t)R, \tag{2.32}$$

if there is also no correlation between $V(t)$, $e_{n1}(t)$ and $i_{n1}(t)$, the PSD of $v_1(t)$ would be

$$S_{v1}(f) \approx S_V(f) + S_{en1}(f) + S_{in1}R^2. \tag{2.33}$$

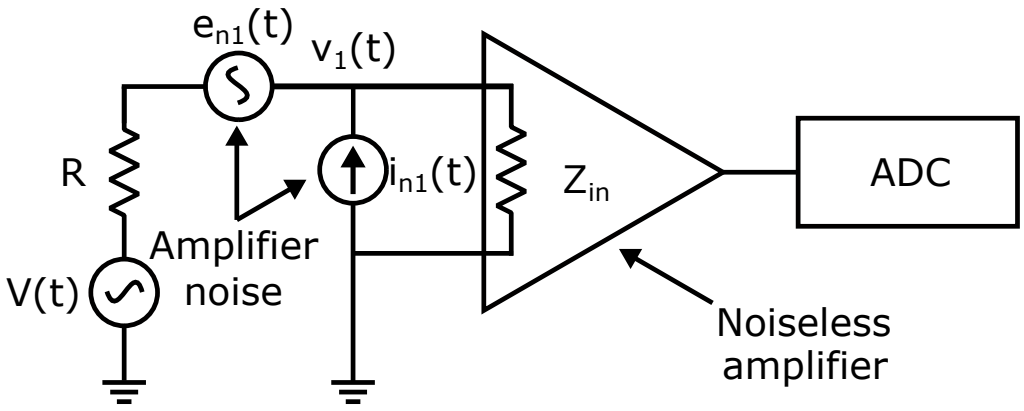

Figure 2.5: Noise circuit model for direct PSD measurement, $V(t)$ is the voltage noise of the DUT, R is the equivalent resistance of the DUT and $v_1(t)$ is the input voltage of the noiseless amplifier.

Where $S_V(f)$ is the voltage PSD of $V(t)$, the voltage noise of the DUT, S_{en1} is the voltage PSD of the equivalent amplifier voltage noise $e_{n1}(t)$ and S_{in1} is the current PSD of the equivalent current noise $i_{n1}(t)$. If

$$S_V(f) >> (S_{en1}(f) + S_{in1}R^2), \tag{2.34}$$

then the PSD of $v_1(t)$ would be

$$S_{v1}(f) \approx S_V(f), \tag{2.35}$$

and thus the direct measurement with the voltage amplifier would be sufficient for acquiring the PSD of the DUT.

2.5.2 Cross correlated measurement of the voltage power spectral density

CSD measurements are warranted when the equivalent voltage noise of the available amplifiers is too large for direct measurement of DUT PSD, allowing for the PSD of the DUT's noise voltage to be measured even when it's noise power is much smaller than that of the amplifiers' equivalent voltage noise. In this section we will analyze the quantitative conditions in which a CSD measurement is called for. The setup and circuit model for the voltage cross correlation method is shown in Fig. 2.6.

Under the assumption $Z_{in} >> R$, $e_{n1}(t)$, $i_{n1}(t)$, $e_{n2}(t)$, $i_{n2}(t)$ and $V(t)$ are all uncorrelated with each other, the voltage PSD at the input of amplifiers 1 and 2 to are

$$S_{v1}(f) = S_{en1}(f) + [S_{in1}(f) + S_{in2}(f)]R^2 + S_V(f) \tag{2.36}$$

$$S_{v2}(f) = S_{en2}(f) + [S_{in1}(f) + S_{in2}(f)]R^2 + S_V(f), \tag{2.37}$$

The CSD between $v_1(t)$ and $v_2(t)$ is

$$S_{v1v2} = [S_{in1}(f) + S_{in2}(f)]R^2 + S_V(f). \tag{2.38}$$

We find that the contribution from the voltage noise of the amplifiers $e_{ni}(t)$ has been removed

from the CSD. Under the circumstance that

$$[S_{in1}(f) + S_{in2}(f)]R^2 << S_V(f), \tag{2.39}$$

In practice, this condition holds true for R values that are approximately $1\mathbf{k}\Omega$ or less. Hence,

$$S_{v1v2} \approx S_V(f). \tag{2.40}$$

We can thus conclude that the voltage noise contribution from the amplifiers is excluded when the cross correlated voltage method is used to extract the PSD of the DUT.

2.6 Conclusion

In summary, we have reviewed in this chapter the mathematical description of noise and simple models for Johnson noise and 1/f noise. We have also provided a description of linear amplifier noise models and correlation methods necessary to understand the fundamental techniques of noise measurement applied in the original research work of chapter 4 and 5. Should the reader be interested to learn more about amplifier noise and measurement techniques please refer to [41] for a detailed review.

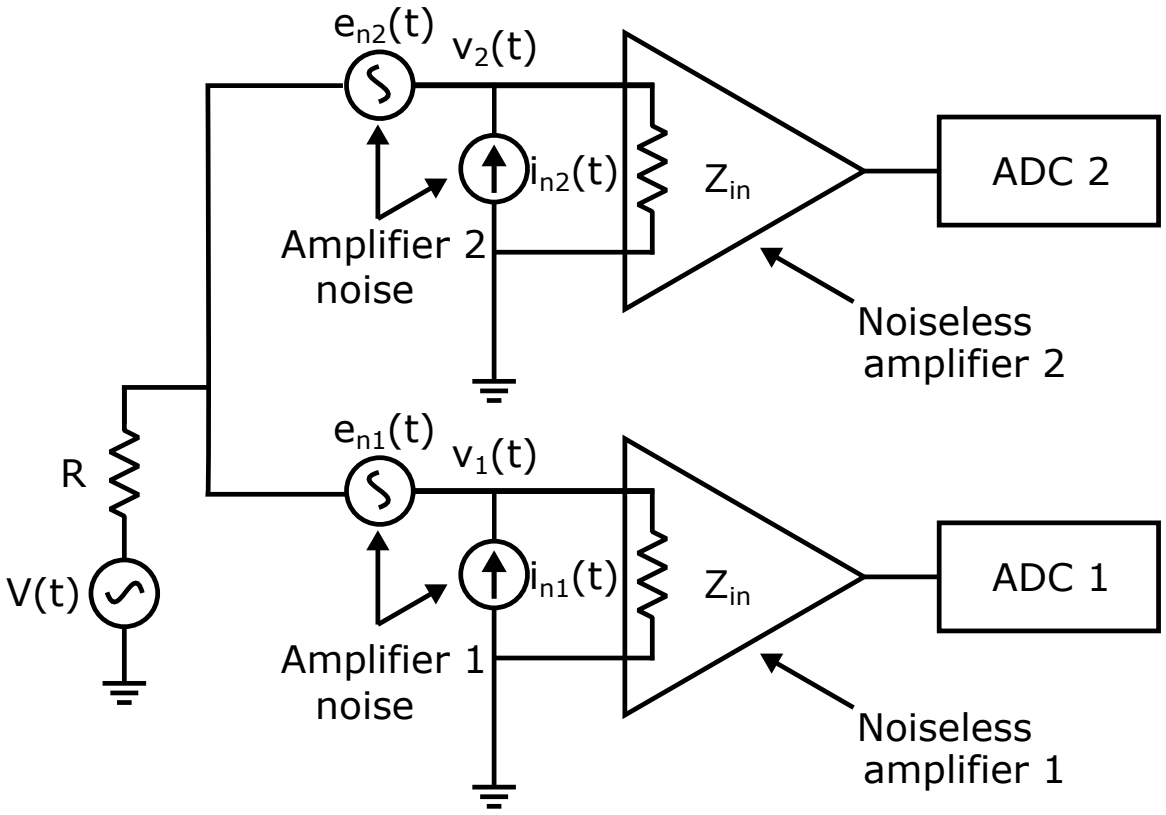

Figure 2.6: Noise circuit model for the voltage cross correlation method of measuring PSD,$V(t)$ is the voltage noise of the DUT, R is the equivalent resistance of the DUT, Where e_{nj}, i_{nj}, Z_{in} $v_j(t)$ and ADC j are the equivalent voltage noise, equivalent current noise, equivalent input impedance, voltage at the output of amplifier and ADC associated to amplifier j respectively, $j = 1, 2$.

Chapter 3

Review of Potentiometric Ion Sensors

Potentiometric ion sensors, a cornerstone in analytical chemistry, have revolutionized the way we detect and measure ions in various environments, from healthcare to environmental analysis and research applications [42,43]. As an illustration, blood analyzers with integrated ion-selective electrodes (ISEs) perform over a billion measurements each year on electrolytes such as K^+, Na^+, Cl^-, Ca^{2+}, Li^+, Mg^{2+}, and CO_3^{2-} [44]. These sensors have significantly improved the efficiency and accuracy of ion concentration measurements, highlighting their vital role across various fields. All potentiometric ion sensors are composed of an ion-selective electrode (ISE) and a reference electrode (RE). By comparing the electrochemical potential of the ISE to that of the RE, the activity or concentration of the ion of interest can be measured.

This review serves to acquaint the reader with the essential electrochemistry concepts

underpinning the subsequent chapters of this work. The chapter commences by introducing the concept of a RE, elucidating the RE's pivotal role in all electrochemical measurements. It then delves into a comprehensive exploration of three distinct types of REs: the standard hydrogen electrode (SHE), the saturated calomel electrode (SCE), and the silver chloride RE. Lastly, a discussion unfolds on the operational principles of the traditional ISE and the ion-sensitive field-effect transistor (ISFET).

3.1 Review of reference electrodes

A RE is employed to measure the electrical potential within a liquid analyte, typically water, containing ions as charge carriers. An effective RE ensures that the measured electrical potential of the analyte remains constant over time, irrespective of the ion species or their concentration within the analyte. We start by addressing a common, yet naive question: Why should we not use a noble metal like platinum or gold as a RE? Metals have electrons as charge carriers, while liquid analytes have ions as charge carriers. If we closely inspect the interface between a metal and a liquid analyte (Fig. 3.1), at low potentials, since electrons cannot travel into the liquid analyte and ions cannot travel into the metal, an electrical double layer is formed on the surface. Consequently, the metal and liquid analyte can only be capacitively coupled, resulting in a highly unstable interface potential. For a stable interface potential to be established, the impedance between the metal and the analyte must be minimized. This is typically achieved through a redox (reduction-oxidation) reaction at

the surface of the interface. As such, we will discuss three different types of REs based on the interface redox reaction of the SHE, SCE and the silver chloride electrode.

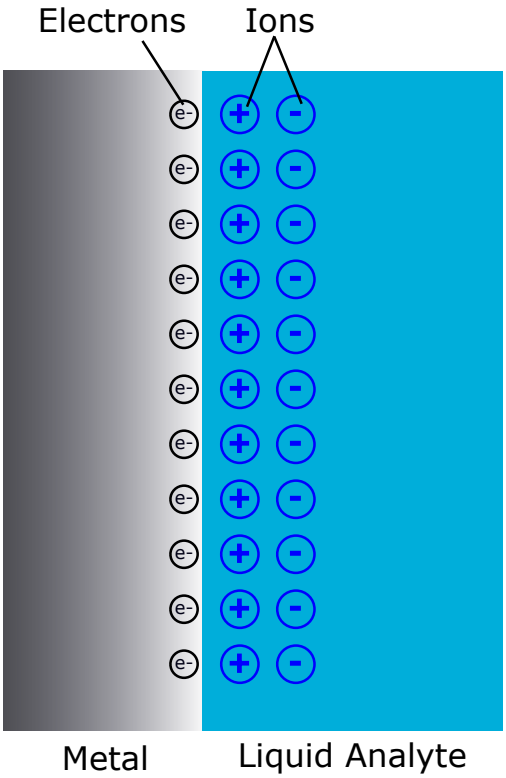

Figure 3.1: Schematic representation of the capacitive double layer at the interface between an electrode and an electrolyte.

3.1.1 Standard hydrogen electrode

In 1893, Max Le Blanc, a German physical chemist demonstrated that bubbling hydrogen gas around a platinum electrode inside an acidic solution gave rise to a stable electrochemical potential [45]. In fact, due the SHE's stability and reproducability, it is the standard potential against which all other electrochemical potential are compared [46].

The SHE is based on the redox reaction involving hydrogen gas and hydrogen ions in solution. The SHE consists of a platinum electrode immersed in a solution with a hydrogen ion concentration of 1 M (ie. a highly acidic condition of pH = 0), where HCl is typically used. Hydrogen gas is bubbled through the solution at a pressure of 1 atmosphere. The platinum electrode acts as a catalytic surface for the hydrogen gas to adsorb and equilibrate with the hydrogen ions in solution. A salt bridge, typically KNO_3 or KCl, is used to connect to the analyte.

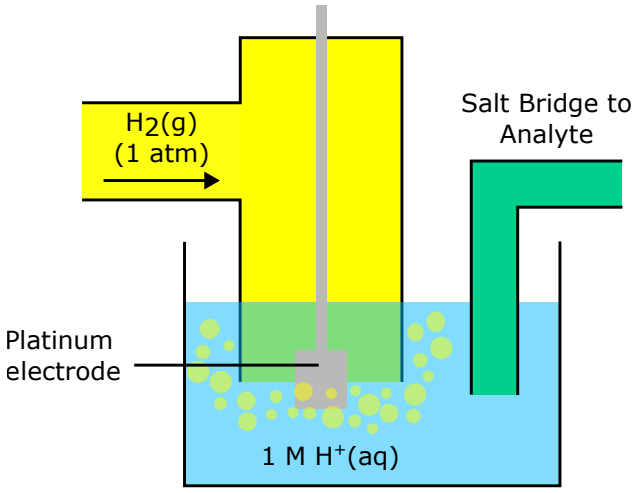

Figure 3.2: Diagram of the Standard Hydrogen Electrode. The SHE consists of a platinum electrode immersed in a 1 M HCl solution with hydrogen gas bubbled through it at a pressure of 1 atm.

The overall redox reaction at the metal-aqueous interface can be represented as:

$$\mathrm{H}_2(g) \rightleftharpoons 2\mathrm{H}^+(aq) + 2e^-$$

At equilibrium, the potential of the SHE is determined by the Nernst equation:

$$E_{\mathrm{SHE}} = E^{\circ}_{\mathrm{SHE}} + \frac{RT}{2F} \ln\left(\frac{[\mathrm{H}^+]^2}{p_{\mathrm{H_2}}}\right)$$

where E°_{SHE} is the standard electrode potential (0 V by definition), $R = 8.31$ J K^{-1} mol^{-1} is the universal gas constant, T is the temperature in Kelvin, $F = 9.65 \times 10^4$ C mol^{-1} is the Faraday constant, $[\mathrm{H}^+]$ is the concentration of hydrogen ions and $p_{\mathrm{H_2}}$ is the partial pressure of hydrogen gas. With the standard conditions defining the $[\mathrm{H}^+]$=1 M and $p_{\mathrm{H_2}}$= 1 atm, we get $E_{\mathrm{SHE}} = 0$ V.

Although the SHE provides a highly stable electrochemical potential, it is not often used due to the complexity associated with setting up the electrode. A constant supply of hydrogen gas and highly concentrated acid solutions pose safety risks that most laboratories are not equipped to handle.

3.1.2 Saturated calomel electrode

The structure of the SCE is demonstrated in Fig. 3.3, consisting of a Hg electrode immersed in a slurry mixture of liquid Hg, solid powder KCl, and solid powder $\mathrm{Hg_2Cl_2}$ (calomel), with a small hole to allow for ionic conduction to an outer solution of aqueous saturated KCl. KCl crystals are added to the aqueous KCl mixture to ensure the aqueous solution stays saturated throughout the usage period. A porous glass frit allows for ionic conduction

between the saturated KCl solution and the analyte solution being measured.

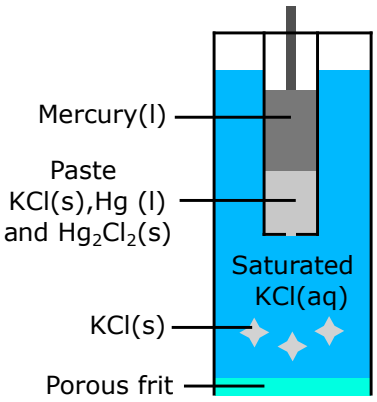

Figure 3.3: Structure diagram of the saturated calomel electrode. The SCE consists of a Hg electrode immersed in a slurry mixture of liqiuid Hg, solid powder KCl, and solid powder Hg_2Cl_2, with a small hole at the bottom. Aqueous KCl, with added KCl crystals, surrounds the Hg and Hg paste layer, terminating at the end with a porous glass frit.

The SCE functions based on the redox reaction between the mercury and calomel:

$$Hg_2Cl_2(s) + 2e^- \rightleftharpoons 2Hg(l) + 2Cl^-(aq) \tag{3.1}$$

The electrode potential of the SCE is measured to be 0.242 V vs SHE at 25°C [47]. The SCE offers several advantages, including its stable potential, ease of use, and relatively low cost. It is significantly less complex to operate compared to the SHE, without the requirement of hydrogen gas. In the past, it was more commonly used in various electrochemical experiments, such as pH measurements, corrosion studies, and electroplating. The public's rising concern with Hg poisoning has contributed to its drop in

popularity, allowing for the silver chloride electrode to take its place as the most common RE.

3.1.3 Silver chloride electrode

The silver chloride (AgCl) or silver/silver chloride (Ag/AgCl) RE is the most widely used RE and is significantly simpler in design when compared to the SHE and SCE. The structure of the AgCl RE is shown in Fig. 3.4. It consists of an Ag wire, which is chlorinated to form AgCl on the surface. The chlorinated Ag wire is immersed in an aqueous KCl solution (typically 3-4 M). The electrode is sealed in a glass tube with a porous glass frit to allow for ionic conduction with the analyte solution being measured.

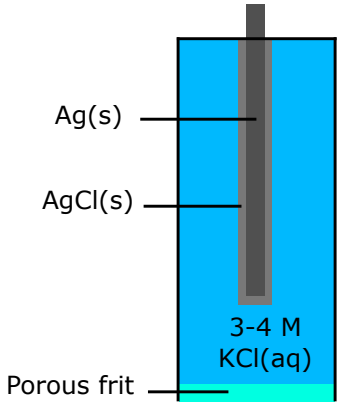

Figure 3.4: Structure diagram of an Ag/AgCl reference electrode. The electrode consists of a silver wire coated with AgCl, immersed in an aqueous KCl solution (typically 3-4 M). The electrode is sealed in a glass tube with a porous glass frit.

The redox reaction at the AgCl interface can be represented as:

$$\mathrm{AgCl}(s) + e^- \rightleftharpoons \mathrm{Ag}(s) + \mathrm{Cl}^-(\mathrm{aq}) \tag{3.2}$$

At equilibrium, the potential of the AgCl RE is determined by the Nernst equation:

$$E_{\mathrm{AgCl}} = E^0_{\mathrm{AgCl}} - \frac{RT}{F} \ln a_{\mathrm{Cl}^-}, \tag{3.3}$$

where E^0_{AgCl} is 0.230 V vs SHE, R is the universal gas constant, T is the temperature in Kelvin, F is the Faraday constant, and a_{Cl^-} is the concentration of chloride ions in the aqueous KCl solution.

The AgCl RE is favored for its stable potential, environmental friendliness, broad temperature range applicability, relatively simple construction, and cost-effectiveness. However, it has certain limitations, including specific storage requirements, unsuitability for non-aqueous solvents, and contamination risks. Despite these drawbacks, it remains a reliable and widely used option in many electrochemical applications when properly maintained.

3.2 Review of traditional liquid-filled ion-selective electrode

An ISE, is an electrode who's electrochemical potential is dependent on the concentration of a specific ion of interest. By comparing the potential of the ISE to that of a RE, the activity or concentration of the ion of interest can be measured.

As can be seen in Fig. 3.5, the structure of a traditional liquid-filled ISE is very similar to that of a AgCl RE, with the glass frit replaced by an ion-selective membrane and an inner filling solution that is dependent on the ion of interest. As an example, a K^+ ISE will have a KCl(aq) inner filling solution, while an NH_4^+ ISE will have NH_4Cl as an inner filling solution. The selective nature of the membrane allows for a potential to build up across the membrane itself. The are two main types of ion selective membranes that are commerically available and widely used. Glass membranes and polyvinyl chloride (PVC) based ionophore membranes.

3.2.1 Glass membranes

Glass membranes are most commonly found in ISEs that are sensitive to H^+ and Na^+. The glass membrane is manly composed of SiO_2 [48]. Adjusting the composition of the glass to also include other oxides, such as Na_2O, CaO, Al_2O_3, Li_2O, and ZnO, the glass membrane can be made sensitive to also K^+, Li^+ and NH_4^+ [49]. In other words, a potential develops

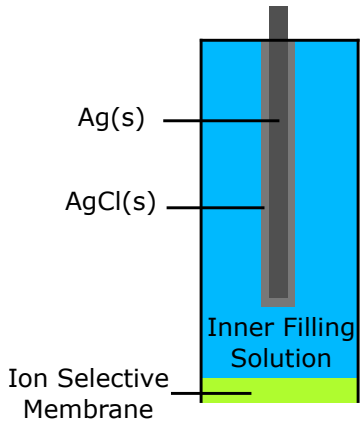

Figure 3.5: Structure diagram of an Ion-selective electrode. The electrode consists of a silver wire coated with AgCl, immersed in an inner filling solutution. The electrode is sealed in a glass tube terminated with an ion-selective membrane.

across the glass membrane in response to a differential in target ion concentration across the membrane.

3.2.2 PVC membranes

PVC-based membranes are the most common type of ion-selective membrane for ions other than H^+ and Na^+. There are four main components: PVC, plasticizer, ionophore, and lipophilic salt. PVC serves as the structural backbone of the membrane, providing mechanical support. Plasticizers, such as dioctyl phthalate, dioctyl sebacate, and o-nitrophenyloctyl ether, allow the membrane to be more flexible and the dissolved lipophilic salt to move freely. The ionophore is the active sensing element that reversibly binds the ion of interest. Lipophilic salts are used to reduce the impedance of the

membrane and give the membrane its permselectivity [50]. The four main components are combined together by dissolving them in a solvent such as tetrahydrofuran (THF) and letting the solvent evaporate.

Traditional liquid-filled ISEs with PVC membranes offer stable and accurate measurements of ion concentrations. However, they require wet storage and regular maintenance, such as refilling internal solutions and frequent calibration. The need for an inner-filling solution and wet storage limits their lifespan to less than six months due to the continuous leaching of components from the membrane. Their limited lifespan, constant need for maintenance, and high costs, render traditional liquid-filled ISEs unsuitable for on-site or in-situ sensing applications.

3.3 Review of ion-sensitive field effect transistor

Ever since the first ISFET was invented by Piet Bergveld in 1970 [51], one of its most successful commercializations has been in semiconductor deoxyribonucleic acid (DNA) sequencing [52]. This has contributed to the exponential decrease in DNA sequencing costs, from $100,000,000 per genome to $600 per genome [53]. As an ISFET is a special type of MOSFET (metal-oxide-semiconductor field-effect transistor), but with the metal gate replaced by an ion-sensitive membrane, electrolyte, and RE, we start by first explaining the working principle of the MOSFET.

3.3.1 Operation principle of the metal-oxide-semiconductor field-effect transistor

A MOSFET is a three-terminal device with a gate, drain, and source. The structure of the MOSFET is shown in Fig. 3.6. Underneath and connecting the metal drain and source contacts is a semiconductor. The gate, sitting on top of the semiconductor, is composed of a metal gate contact and metal oxide. Applying a voltage between the gate and source induces an electric field, which changes the conductance of the semiconductor. This change in conductance can be measured through the drain-source current with a fixed drain-source voltage bias. Quantitatively, the drain-source current at low voltage biases is

$$I_{ds} = \mu C_{ox} \frac{W}{L} (V_{gs} - V_t) V_{ds}, \tag{3.4}$$

where μ is the electron mobility inside of the semiconductor, C_{ox} is the oxide capacity per unit area, W and L are the width and length of the channel respectively [54]. V_t is the threshold voltage and is dependent on both the type of semiconductor and the oxide layer. This drain-source current, gate-source dependency allows for the MOSFET to be an effective transimpedance and transconductance amplifier.

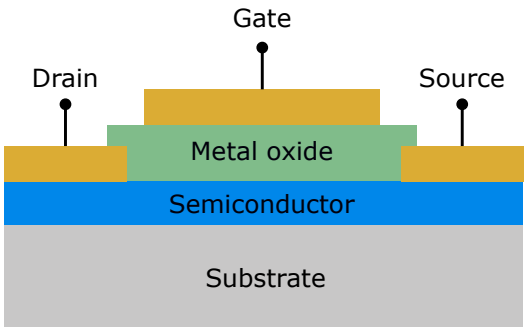

Figure 3.6: Structure diagram of an metal-oxide field-effect transistor. The diagram illustrates the primary components of a MOSFET, including the gate, drain, and source terminals. The semiconductor, which is positioned on top of a substrate to provide mechanical support, connects the metal drain and source contacts. The gate, located above the semiconductor, consists of a metal gate contact and a metal oxide layer.

3.3.2 Operation principle of the ion sensitive field effect transistor

As illustrated in Figure 3.7 and as previously discussed, the ISFET (ion sensitive field effect transistor) is a MOSFET (metal oxide semiconductor field effect transistor) where the gate is replaced by a RE, an electrolyte, and an ion-selective membrane. The ion-selective membrane of ISFETs sensitive to H^+ ions typically consists of a thin oxide layer of Ta_2O_5 or Al_2O_3 due to their high surface buffer capacity for proton uptake and their large dielectric constant compared to SiO_2 [54, 55]. Additionally, graphene ISFETs sensitive to ions such as K^+, Cl^-, Na^+, NH_4^+, NO_3^-, SO_4^{2-}, and HPO_4^{2-} have been demonstrated using a PVC-based ionophore membrane [20]. The concentration of the

target ion inside the electrolyte modulates the potential between the ion-selective membrane and electrolyte, which in turn changes the drain-source current at a fixed drain-source voltage bias. In essence, the ISFET is a transconductance amplifier that amplifies the potential change induced by a change in ion concentration.

When compared to pH ISEs, pH ISFETs have significantly faster response times and higher resolution [56]. Combining these advantages with their miniaturizability and scalability using existing semiconductor technology has facilitated their adoption in the commercial DNA sequencing sector [57].

Graphene ISFETs function effectively like silicon ISFETs but exhibit several notable differences: being gapless, they have an identical threshold voltage V_t for both n-type (electron) and p-type (hole) conduction, referred to as the neutrality point. This results in the low-bias regime of the transistor equation always applying, making saturation unachievable due to the inability to achieve depletion. Additionally, the mobility μ in graphene ISFETs is typically an order of magnitude greater than in silicon ISFETs. Despite these advantages, it remains an open question whether the unique characteristics of graphene ISFETs will lead to their adoption in analytical applications.

3.4 Conclusion

This chapter provided a comprehensive overview of potentiometric ion sensors, focusing on their electrochemical principles and operational mechanisms. It discussed the key

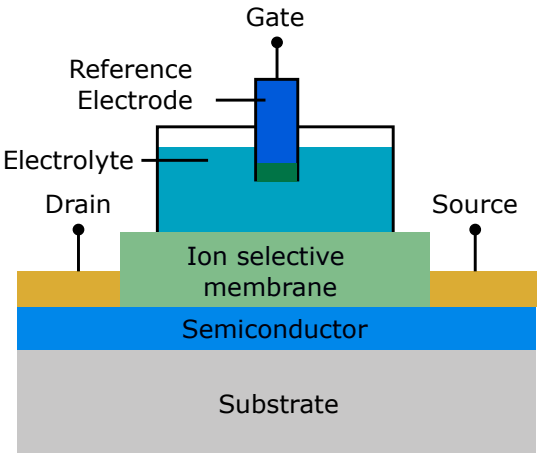

Figure 3.7: Structure diagram of an ion-sensitive field-effect transistor. The diagram illustrates the primary components of an ISFET, including the gate, drain, and source terminals. The semiconductor, which is positioned on top of a substrate to provide mechanical support, connects the metal drain and source contacts. The gate, located above the semiconductor, consists of a reference electrode, electrolyte and ion-selective membrane

characteristics and functionalities of reference electrodes (REs), such as the standard hydrogen electrode (SHE), the saturated calomel electrode (SCE), and the silver chloride electrode (AgCl). While the electrochemical stability of traditional liquid-filled reference electrodes has been extensively studied [58, 59], the long-term stability of planar reference electrodes has received significantly less attention. Hence our discussion of our solid reservoir reference electrode in chapter 6. Furthermore, the chapter elucidated the working principles underlying traditional liquid-filled ion-selective electrodes (ISEs), as well as the advanced technologies of metal-oxide-semiconductor field-effect transistors (MOSFETs) and ion-sensitive field-effect transistors (ISFETs).

Chapter 4

Fluctuation-Dissipation in Thermoelectrics

This chapter presents our theoretical and experimental work, where we expand the fluctuation-dissipation theorem to thermoelectric materials and devices. We begin by theoretically demonstrating the coupling between temperature fluctuations and voltage fluctuations in thermoelectric materials, finding an enhanced voltage fluctuation spectral density $4k_BTR(1+ZT)$ at frequencies below a thermal cut-off frequency f_T, where ZT is the dimensionless thermoelectric device figure of merit. We experimentally measured this enhanced voltage power spectral density in an ultra-fast response ($f_T \sim 1$ kHz) integrated thermoelectric micro-device to experimentally confirm our findings. Measuring the ZT enhanced voltage noise, we experimentally resolve temperature fluctuations with an

amplitude of 0.8 μK Hz^{-1} at a mean temperature of 295 K.[1]

4.1 Introduction

The fluctuation-dissipation theorem [13] relates the fluctuations in a system at thermodynamic equilibrium with the coefficient of irreversible dissipation under an externally applied bias field. In an electrical conductor, the fluctuation-dissipation theorem takes the form of the Johnson-Nyquist noise formula for voltage fluctuations $\langle V^2 \rangle = 4k_B T R \Delta f$, where k_B is Boltzmann's constant, T is absolute temperature, R is the electrical resistance, and Δf is the electrical bandwidth [12, 60]. The resistance R that quantifies the irreversible dissipation of electrical conduction also determines the amplitude of voltage fluctuations at equilibrium. Since it's formal statement, the fluctuation-dissipation theorem has been extended to various physical systems, including the quantum optical regime [14].

Considering fluctuations in an electrical conductor further, fundamental excitations in condensed matter carry not only charge, but other physical quantities such as, for example, heat, spin, and pseudo-spin. The *thermoelectric* response of a conductor is a result of the correlated transport of charge and heat by fundamental excitations. In the simplest scenario, the Seebeck coefficient S is a measure of the mean entropy carried per unit charge e, and the

[1] This chapter is based on the following published article: **Tran, Ngoc Anh Minh**, et al. "Fluctuation-dissipation in thermoelectric sensors." Europhysics Letters 141.2 (2023): 26002.

Peltier coeffiecient $\Pi = TS$ is a measure of the mean thermal energy carried per unit charge e [61–63]. Surprisingly, the fluctuation-dissipation theorem as it applies to a thermoelectric material has not been investigated to date.

In this paper, we apply the fluctuation-dissipation theorem to derive a generalized Johnson-Nyquist formula for thermoelectrics, revealing a modification in the spectral density of fluctuations that is dependent on the dimensionless, material thermoelectric figure of merit $zT = \Pi S/\kappa\rho$ (not to be confused with device ZT, see Eq. (4.11)), where κ is the thermal conductivity and ρ is the electrical resistivity. Using integrated, wide-bandwidth, thermoelectric cooling micro-devices [64], we measure the spectral density of voltage fluctuations and find agreement with the generalized Johnson-Nyquist formula for thermoelectrics. In the spirit of the fluctuation dissipation theorem, experimental impedance spectroscopy is further used to explicitly test the correspondence between irreversible transport coefficients and equilibrium fluctuations in a thermoelectric material.

4.2 Theory

Let us consider an electrical current I_e and a heat current I_Q in a thermoelectric sample of length L and cross-sectional area A in the presence of a time-dependent potential difference

ΔV and temperature difference ΔT,

$$\begin{aligned} I_e &= L'_{11}\Delta V + L'_{12}\frac{\Delta T}{T} \\ I_Q &= L'_{21}\Delta V + L'_{22}\frac{\Delta T}{T} + C'_Q\frac{\partial}{\partial t}\Delta T, \end{aligned} \tag{4.1}$$

where $L'_{ij} = (A/L)L_{ij}$ are the extensive transport coefficients, satisfying Onsager's reciprocal relation $L'_{12} = L'_{21}$. The intensive transport coefficients L_{ij} are related to electrical conductivity σ, Seebeck coefficient S, thermal conductivity κ,

$$\sigma = L_{11}, \quad S = -\frac{1}{T}\frac{L_{12}}{L_{11}}, \quad \kappa = \frac{1}{T}\frac{L_{22}L_{11} - L_{12}L_{21}}{L_{11}}. \tag{4.2}$$

The dynamical response of the thermoelectric depends upon the extensive heat capacity $C'_Q = \partial U/\partial\Delta T$, where U is the heat transported across the length L of the thermoelectric.

The transport Eq. (4.1) can be compactly expressed with a generalized potential $\tilde{\mathbf{V}}$, generalized flux $\tilde{\mathbf{I}}$, and generalized conductance $\mathbb{G}$,

$$\begin{aligned} \tilde{\mathbf{I}} &= \mathbb{G}\tilde{\mathbf{V}}, \\ \begin{bmatrix} I_e(f) \\ I_Q(f) \end{bmatrix} &= \begin{bmatrix} L'_{11} & L'_{12} \\ L'_{21} & L'_{22} + i2\pi f T C'_Q \end{bmatrix} \begin{bmatrix} \Delta V(f) \\ \Delta T(f)/T \end{bmatrix}, \end{aligned} \tag{4.3}$$

where the Fourier transform $x(f) = \int e^{2\pi i f t}x(t)dt$ is used to work in the frequency domain.

The fluctuation-dissipation theorem applied to the generalized potential $\tilde{\mathbf{V}}$ gives,

$$S_{\alpha,\beta} = 4k_B T \mathrm{Re}\left[\mathbb{G}^{-1}_{\alpha,\beta}\right], \tag{4.4}$$

where the spectral density of fluctuations $S_{\alpha,\beta}(f)$ is defined,

$$S_{\alpha,\beta}(f) = \frac{2}{\mathcal{T}}\langle \tilde{\mathbf{V}}_\alpha(+f)\tilde{\mathbf{V}}_\beta(-f)\rangle, \tag{4.5}$$

where $\langle x\rangle$ denotes the ensemble average of x, and $\mathcal{T} = 1/\Delta f$ is the reciprocal bandwidth. From an experimental perspective, $\mathcal{T}$ is the temporal duration of a measurement [39], while in theoretical analysis $\mathcal{T}$ is the period in the periodic model of a stationary physical system [65].

The spectral density $S_T(f) = 2\mathcal{T}^{-1}\langle \Delta T(+f)\Delta T(-f)\rangle$ of the temperature fluctuations across the thermoelectric is,

$$S_T(f) = 4k_B T^3 \mathrm{Re}[\mathbb{G}^{-1}_{22}] = 4k_B T^2 \frac{G_T^{-1}}{1+(f/f_T)^2}, \tag{4.6}$$

where $G_T = \kappa A/L$ is the thermal conductance and $2\pi f_T = G_T/C'_Q$ is the thermal cut-off frequency. The total integrated temperature fluctuation, $\langle(\Delta T)^2\rangle = \int_0^\infty S_T df = k_B T^2/C'_Q$, in accordance with the result expected from general considerations of statistical mechanics [66].

The spectral density of the voltage fluctuations $S_V(f) = 2\mathcal{T}^{-1}\langle \Delta V(+f)\Delta V(-f)\rangle$ across

the thermoelectric is,

$$S_V(f) = 4k_BT\mathrm{Re}[\mathbb{G}_{11}^{-1}] = 4k_BTR_0 + S^2S_T(f). \tag{4.7}$$

There are voltage fluctuations of Ohmic origin proportional to the transport coefficient $R_0 = L_{11}'^{-1}$, and voltage fluctuations that originate with temperature fluctuations coupled via the thermoelectric coefficient S. An independent analysis showing the coupling between temperature gradient and electric field fluctuations is shown in the Supplemental Material [67].

Combining the results of Eq. (4.6) and Eq. (4.7), we arrive at the central theoretical result for voltage fluctuations in a thermoelectric,

$$S_V(f) = 4k_BTR_0\left[1 + \frac{zT}{1 + (f/f_T)^2}\right]. \tag{4.8}$$

In the high-frequency limit above the thermal cut-off frequency, $f \gg f_T$, the usual Johnson-Nyquist formula for spectral density of voltage fluctuations applies, $S_V = 4k_BTR_0$. The spectral density of temperature fluctuations diminish $S_T(f) \propto f^{-2}$ for $f \gg f_T$. In contrast, in the low-frequency limit below thermal cut-off, $f \ll f_T$, there is an enhancement in spectral density of voltage fluctuation beyond the usual Johnson-Nyquist result, $S_V = 4k_BTR_0(1 + zT)$. The low-frequency spectral density of temperature fluctuations, $S_T \to 4k_BT^2G_T^{-1}$, contributes to the observable voltage fluctuations via

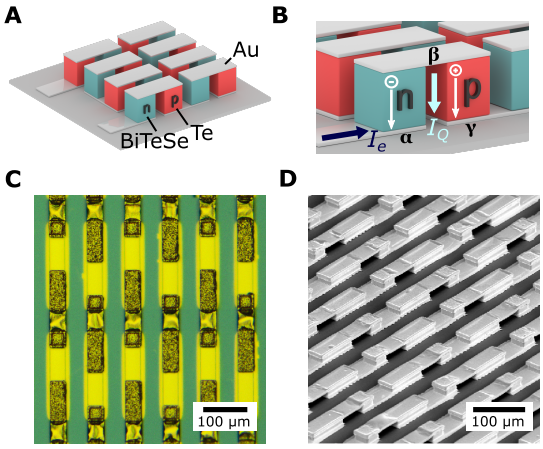

Figure 4.1: Integrated thermoelectric cooler. **A** Illustration of the alternating n-type BiTeSe and p-type Te thermoelectric legs with Au electrodes, arranged in a serpentine, series pattern on a substrate. **B** Diagram demonstrating the direction of heat current I_Q downward in both n-type and p-type material as electrical current I_e passes from left to right in the Π architecture of an n/p pair.**C** Optical microscope image of the fabricated thermoelectric micro-device. **D** Oblique angle scanning electron microscope image of the fabricated thermoelectric micro-device.

thermoelectric coupling. The dimensionless zT determines the relative enhancement of voltage noise beyond the Johnson-Nyquist result. Thermoelectric noise enhancement is thus anticipated in materials with large Seebeck coefficient S, large electrical conductivity σ, and small thermal conductivity κ.

To confirm our theoretical findings, we measured the voltage noise spectral density of integrated, wide-bandwidth, thermoelectric cooling micro-devices. The devices consist of a series network of $L = 10$ μm thick n-type ($Bi_2(Te_{0.95}Se_{0.05})_3$), abbreviated as BiTeSe) and p-type (pure Te) thermoelectric materials, with Au contacts, arranged in serpentine fashion on a Si substrate, as shown in Fig. 4.1A. A Π architecture is adopted, Fig. 4.1B, such that the

contra-oriented electrical current I_e in each leg results in co-oriented heat current I_Q in each leg. A microfabricated structure, Fig. 4.1C and Fig. 4.1D, was used to achieve a high thermal cut-off frequency $f_T \sim 1$ kHz, as confirmed by experiment. The cross-sectional areas of the p-type and n-type legs are $A_p = 85\ \mu\text{m} \times 30\ \mu\text{m}$ and $A_n = 30\ \mu\text{m} \times 30\ \mu\text{m}$, respectively. The device systematically studied in our work consisted of 112 series leg pairs. Further details concerning the design and fabrication of wide-bandwidth thermoelectric micro-coolers have been previously reported [64]. The spectral density of voltage fluctuations for a thermolectric material in Eq. (4.8) can be extended to a thermoelectric device consisting of a series of N identical leg pairs.

Consider first the voltage fluctuation across a single leg pair in the Π geometry of Fig. 4.1B. Due to the effective thermal short-circuit between points α and γ from the substrate thermal conductivity, the fluctuation in temperature difference $\Delta T = T_\beta - T_\alpha = T_\beta - T_\gamma$ across the n-type and p-type legs have a spectral density,

$$S_T(f) = 4k_B T^2 \frac{(G_n + G_p)^{-1}}{1 + (f/f_{T,\Pi})^2}, \tag{4.9}$$

where $G_n = \kappa_n A_n/l$, $G_p = \kappa_p A_p/l$ are the thermal conductances of each leg, l is the length of each leg, and the thermal cut-off frequency $2\pi f_{T,\Pi} = (G_n + G_p)/C'_{Q,\Pi}$ where $C'_{Q,\Pi}$ is the total heat capacity for establishing a temperature difference ΔT across the leg pair. The voltage fluctuations across the n-leg $(\alpha - \beta)$ and p-leg $(\beta - \gamma)$ that arise from thermoelectric

transduction of temperature fluctuations are correlated, and given by $(S_p - S_n)^2 S_T(f)$. The voltage fluctuations across distinct leg pairs are not correlated, and thus the expected spectral density of voltage fluctuation across the series of N leg pairs in our thermoelectric device is

$$S_V(f) = 4k_B T N(R_n + R_p)\left[1 + \frac{ZT}{1 + (f/f_{T,\Pi})^2}\right], \tag{4.10}$$

where R_i and S_i are the electrical resistance and Seebeck coefficient of the i-type leg, i=n,p, and ZT is the thermoelectric device figure of merit,

$$ZT = \frac{T(S_p - S_n)^2}{(R_n + R_p)(G_n + G_p)}. \tag{4.11}$$

The voltage fluctuation of the thermoelectric micro-device, Eq. (4.10), differs from the voltage fluctuation of a thermoelectric material, Eq. (4.8), albeit sharing a similar form. Note that the *device* figure of merit ZT is not the sum of the constituent *material* figures of merit zT, due to the correlated temperature difference ΔT across p- and n-legs [62].

4.3 Methods and results

The voltage power spectral density $S_V(f)$ was measured using a correlation method, as shown in Fig. 4.2A. The voltage across two terminals of a series of p/n leg pairs was measured simultaneously with two cascaded voltage amplifiers. Each cascade consisted of two identical

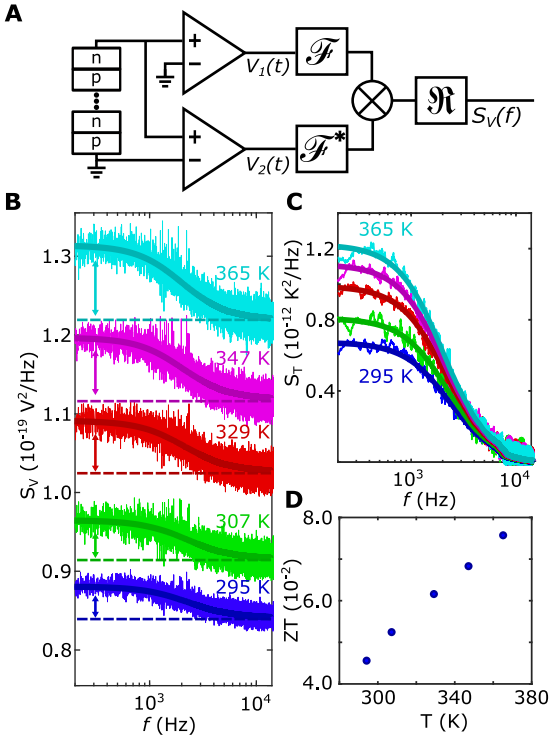

Figure 4.2: Voltage and temperature fluctuations. **A** Circuit diagram of the cross-periodogram method used to estimate the spectral density $S_V(f)$ of voltage fluctuations across the thermoelectric micro-device. Independent measurements $V_1(t)$ and $V_2(t)$ are acquired and digitally Fourier transformed to reconstruct S_V from the cross-spectral density. **B** Voltage spectral density $S_V(f)$ versus frequency f of the thermoelectric micro-device measured at a substrate temperature T from 295 K to 365 K. Solid dark lines show a fit to theoretical spectral density of Eq. (4.10). The Ohmic Johnson-Nyquist contributions $4k_BTN(R_n + R_p)$ are indicated with dashed lines, and the excess spectral density $\Delta S_V = S_V - 4k_BTN(R_n + R_p)$ arising from thermoelectric coupling is indicated with vertical arrows. **C** The temperature fluctuation spectral density $S_T(f) = \Delta S_V / S^2$ versus frequency f, using the independently measured, temperature dependent, effective Seebeck coefficient S. A 40 Hz running average was applied to S_T for visual clarity, and a model fit to Eq. (4.9) is shown. **D** The thermoelectric micro-device figure of merit $ZT = \lim_{f \to 0} \Delta S_V / (S_V - \Delta S_V)$ versus substrate temperature T.

voltage pre-amplifiers (LI-75, NF Corp.) with 40 dB total gain. The voltages $V_1(t)$ and $V_2(t)$ were digitized (DT-9847, Data Translation) and the cross-spectral density estimated using the cross-periodogram method [39]. To suppress the uncorrelated amplifier noise in $V_1(t)$ and $V_2(t)$, we averaged 7.5×10^4 periodograms, with 2.15×10^5 samples/periodogram acquired at a sampling rate of 2.15×10^5 samples/s, for over 20 hours of acquisition time per spectral density measurement. The micro-device was placed in a series of metal boxes for electrical and thermal isolation, open-loop resistive heating was applied to vary the sample substrate temperature T, and a thermistor was used to measure the T, which varied by less than ± 1 K over the duration of each measurement.

The spectral density of the voltage across the thermoelectric is reconstructed as $S_V = 2\mathcal{T}^{-1}\mathrm{Re}\left\{V_1(f)V_2^*(f)\right\}$. The comparatively high thermal cut-off frequency, $f_{T,\Pi} \sim 1$ kHz, is essential to avoid measurements in the extremely low frequency (ELF, $f < 30$ Hz) band where amplifier $1/f$ noise is prohibitively large. Frequency independent measurement system response over the bandwidth 200 Hz $< f <$ 20 kHz was confirmed using a resistor of $R = 25.9\ \Omega$ (see Supplemental Material [67]). The gain in the noise measurement system was calibrated with an $R = 8.20\ \Omega$ resistor at $f = 1.7$ kHz.

The measured voltage spectral density, $S_V(f)$, as a function of frequency f, is shown in Fig. 4.2B, alongside a numerical fit to Eq. (4.10). The measurements were conducted with the thermoelectric substrate temperature, T, varied from 295 K to 365 K using an external resistive heater, with the temperature monitored via a thermistor. The dashed horizontal

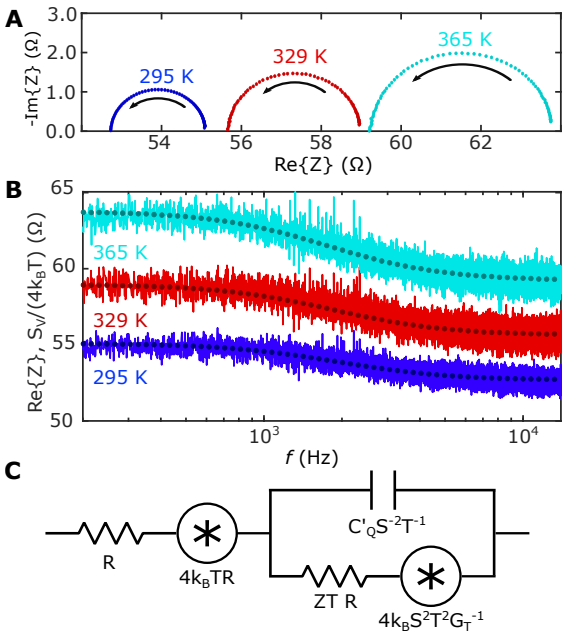

Figure 4.3: Impedance and noise spectroscopy. **A** Nyquist plot of the measured impedance, $-\mathrm{Im}\{Z\}$ versus $\mathrm{Re}\{Z\}$ at T =295 K,329 K, and 365 K, over the frequency 100 Hz $< f <$ 100 kHz. The semi-circle arrows direction indicates an increase in frequency. **B** A comparison of the measured dissipative impedance $\mathrm{Re}\{Z\}$ (darker circles) and the measured voltage spectral density normalized to impedance units, $S_V/4k_BT$, (thin line) versus frequency f. **C** Model circuit for a thermoelectric, including Ohmic and thermoelectric dissipative elements, Ohmic and thermolectric fluctuation sources, and effective capacitance.

lines represent the Ohmic Johnson-Nyquist noise contribution, $4k_BTN(R_n + R_p)$. The total resistance, $N(R_n + R_p)$, thermal cutoff frequency, f_T, and thermoelectric device figure of merit, ZT, were extracted from the fit of the measured S_V to Eq. (4.10). An enhancement in voltage fluctuations, $\Delta S_V = S_V - 4k_BTN(R_n + R_p)$, is observed in the low-frequency limit, $f \ll f_T$, compared to the high-frequency limit, $f \gg f_T$, as indicated by the vertical arrows.

The spectral density of temperature fluctuations, $S_T = \Delta S_V / S^2$, was determined using the effective, temperature dependent, Seebeck coefficient $S = S_p - S_n$ inferred from measurements of BiTeSe and Te thin films (see Supplemental Material). For example, at $T = 298$ K, $S_p = 194\ \mu\text{VK}^{-1}$, $S_n = -44\ \mu\text{VK}^{-1}$ and $S = 238\ \mu\text{VK}^{-1}$. The experimentally determined spectral density of temperature fluctuations, S_T, is shown in Fig. 4.2C versus substrate temperature T, along with a model fit to Eq. (4.9). At $T = 295$ K, the experimentally resolved amplitude of temperature fluctuations is $\delta T = S_T^{1/2} = 0.8\ \mu\text{KHz}^{-1/2}$, corresponding to a relative fluctuation amplitude $\delta T/T = 3 \times 10^{-9}\ \text{Hz}^{-1/2}$. In the context of thermometry, our findings show that a thermoelectric micro-device can be used to measure temperature differences as small as the fundamental fluctuations described by the fluctuation-dissipation theorem.

The micro-device figure of merit ZT can be determined from the frequency dependent voltage noise S_V, with $ZT = \lim_{f \to 0} \Delta S_V / (S_V - \Delta S_V)$. The figure of merit ZT versus substrate temperature T is shown in Fig. 4.2D, where ZT was determined from a fit of the experimentally measured S_V to Eq. (4.10). As anticipated, ZT increases with substrate temperature T.

The fluctuation dissipation theorem identifies the equivalency of the coefficient for fluctuation at thermal equilibrium and the coefficient for dissipative transport. We therefore investigated this equivalency for thermoelectrics. The transport Eq. (4.1) leads to

a frequency dependent electrical impedance,

$$Z(f) = \frac{\Delta V}{I_e} = R\left(1 + \frac{ZT}{1 + if/f_{T,\Pi}}\right), \tag{4.12}$$

where $R = N(R_n + R_p)$ for our thermoelectric micro-device. The impedance of Eq. (4.12) is the basis for impedance spectroscopy of thermoelectrics, which have evolved in complexity [68–72]. The thermoelectric cooling device impedance was measured using a lock-in amplifier (MLFI 500kHz, Zurich Instruments) with an AC current bias I_e of 100 μA amplitude over a frequency range 100 Hz $< f <$ 100 kHz. The Nyquist plot of measured $-\mathrm{Im}\{Z\}$ versus $\mathrm{Re}\{Z\}$ is shown in Fig. 4.3A at T =295 K, 329 K, and 365 K. The semi-circle characteristic of first-order response is evident in the Nyquist plot, and a numerical fit to the simple model of Eq. (4.12). A direct comparison of the measured dissipative impedance coefficient $\mathrm{Re}\{Z\}$ and the measured normalized voltage fluctuation spectral density $S_V/4k_BT$ is shown in Fig. 4.3B. Our experiments are in good agreement with the fluctuation dissipation theorem as applied to the effective electronic sector of the transport equations, $\mathrm{Re}\{Z\} = S_V/4k_BT$. The thermoelectric coupling thus simultaneously enhances both the spectral density of voltage fluctuations and the electrical impedance.

Assembling our findings, a simple equivalent electrical transport model for a thermoelectric element is shown in Fig. 4.3C, using simplified notation. The model includes the Ohmic resistance R and associated Johnson-Nyquist fluctuations of spectral

density $4k_BTR$, a resistance $ZT \cdot R = TS^2G_T^{-1}$ of thermoelectric origin with an associated spectral density of voltage fluctuations $4k_BTR \cdot ZT = 4k_BS^2T^2G_T^{-1}$. The frequency dependence of thermal contributions to impedance and voltage fluctuations is accounted for with the inclusion of an effective capacitance $C_T = C'_QT^{-1}S^{-2}$ of thermal origin, with cut-off frequency $2\pi f_T = G_T/C_T$.

4.4 Conclusion

In conclusion, we have demonstrated how the fluctuation dissipation theorem can be extended to thermoelectrics, revealing the role of temperature fluctuations in the modification of the renowned Johnson-Nyquist formula. Our work establishes a quantitative understanding of temperature fluctuations in thermoelectrics, defining an important physical limit for micro-scale thermoelectric thermometery in, for example, intracellular thermometry [73]. Finally, we note that our results can be generalized to include other physical quantities carried by fundamental excitations in a conductor. For example, spin-orbit coupling can result in fundamental excitations that carry charge and spin, and the correlated transport of charge and spin can in principle lead to a modification of the observable spectral density of voltage fluctuations. Moreover, the spectral density of voltage fluctuations may give insight into the spectral density of spin fluctuations.

Chapter 5

Graphene Field Effect Transistor Scaling for Ultra-low-noise Sensors

In this chapter we present our work on the measurement and characterization of $1/f$ noise in graphene field effect transistor sensors. We demonstrate a straightforward technique to reduce $1/f$ noise by scaling the active area of graphene field effect transistor (GFET) sensors. We measured $1/f$ noise in GFETs with sizes ranging from 5 μm$\times$5 μm to 5.12 mm$\times$5.12 mm, achieving a reduction in $1/f$ noise by more than five orders of magnitude. This led to the lowest normalized graphene $1/f$ noise parameter recorded to date, 5×10^{-13}. Furthermore, we developed a sulfate ion sensor with an unprecedented resolution of 1.2×10^{-3} log molar concentration units.[1]

[1]This chapter is based on the following published article: **Tran, Ngoc Anh Minh**, et al. "Graphene field effect transistor scaling for ultra-low-noise sensors." Nanotechnology 32.4 (2020): 045502.

5.1 Introduction

The application of field effect transistors (FETs) to the measurement of analytes began with Bergveld's invention [51] of the ion sensitive field effect transistor (ISFET). Since the invention of the graphene field effect transistor [18], the exquisite sensitivity of monolayer graphene conductivity to surface adsorption phenomena has been used to demonstrate sensing of molecules in the ambient gas phase [74], alkali atoms in ultra-high vacuum [75], ions in an acqueous environment [76] and biomolecules in physiological solutions [77]. Graphene FETs are particularly well suited as sensors due to the high conductive gain achievable with high charge carrier mobility $\mu > 1000$ cm^{2}V^{-1}s^{-1} and ideal coupling between charge carriers in an atomic layer and the external environment. The chemical inertness of the graphene surface leads to the inherent insensitivity of graphene FETs to analytes [76, 78], allowing the selectivity of graphene FET response to a particular target analyte to be achieved by functionalization. A wide variety of graphene FET sensors have subsequently been developed, including pH sensors operating at thermodynamic and quantum capacitance limits [55, 76, 79], alkali ion sensors [20, 80, 81], toxic chemical sensors [82], DNA sensors [83–87] and protein sensors [88–93]. The majority of graphene sensor work has focussed on optimizing sensitivity $s = \partial X/\partial \log a$, where X is either the FET channel current I, voltage V or resistance R and a is the activity of the analyte, by rational design of the graphene functionalization protocol. Quantitative analytical measurements require sensors with optimized signal to noise ratio (SNR), which has

received comparatively less attention [55, 87].

The minimum measurable change in analyte activity is the sensor resolution $r = k\sqrt{\langle \Delta X^2 \rangle}/s$ where $\sqrt{\langle \Delta X^2 \rangle}$ is the rms noise of the FET channel current, voltage or resistance and k is a confidence factor [94]. At low-frequencies relevant to analyte concentration measurement, $f < 1$ Hz, graphene FET channel noise is dominated by $1/f$ noise, wherein the power spectral density (PSD) of the channel current, voltage or resistance $S_X \propto 1/f$. The $1/f$ noise of graphene FETs has been measured in devices produced by mechanical exfoliation [36] and chemical vapour deposition (CVD) methods [95] on various substrates. Several physical mechanisms have been identified as sources of $1/f$-noise in graphene FETs, including charge density fluctuation [96] and mobility fluctuation [97] within the bulk graphene channel. Recently, contact resistance fluctuations [98] have been identified as the dominant source of $1/f$ noise in high-mobility graphene FETs with $\sim 1 - 10$ μm channel length in two-point, four-point, and non-invasive four-point geometries. However, the relative magnitude of contact resistance fluctuations $\langle \Delta R_c^2 \rangle$ and bulk graphene channel resistance fluctuations $\langle \Delta R^2 \rangle$ is not expected to be invariant with absolute device size. For example, contact resistance is inversely proportional to contact perimeter due to current crowding at metal-graphene junctions, and thus the ratio of contact resistance to channel resistance in a two-point $L \times L$ square geometry is $R_c/R \propto 1/L$, such that contact resistance is negligible for a sufficiently large device. The scaling of graphene FET noise with absolute device size has not been

systematically investigated to date.

In this work, we report systematic measurements of the low-frequency noise of a series of graphene FETs with active area spanning more than six orders of magnitude from $L^2 = 25\ \mu\text{m}^2$ up to 26 mm^2. The scaling of graphene FET channel voltage noise is found to abide by Hooge's emprirical scaling law [99],

$$S_V = \frac{V_0^2}{f}\frac{\alpha_H}{N}, \tag{5.1}$$

where $V_0 = I_0 R_{4pt}$ is the dc voltage across the FET, f is the frequency, α_H is the Hooge coefficient, and $N = nL^2$ is the total number of charge carriers in the graphene channel, with n being the charge carrier density. By scaling the active area of graphene FETs up to $L^2 = 26$ mm^2, we observe the lowest normalized noise parameter $K = S_V f/V_0^2 = 5 \times 10^{-13}$ in a graphene FET reported to date. A graphene FET sensor has SNR $\propto 1/K$, and thus improved sensor performance can be achieved by scaling graphene FETs to *larger* channel area, contrary to the familiar Moore's law of FET scaling to *smaller* channel area to maximize computational density in digital electronics.

5.2 Methods and results

We fabricated graphene FETs from large-area, poly-crystalline, monolayer graphene synthesized on Cu via CVD. The graphene was transferred to a parylene/SiO_2/Si substrate

and patterned by lithography and reactive ion etching (RIE) into van der Pauw geometries with size $L = 5$ μm - 5120 μm, as shown in Fig. 5.1. The optical microscope images of our devices are shown in Fig. 5.1C, the gold appearance of the graphene is a result of optical reflection from 130 nm of parylene C on 300 nm of SiO_2 on silicon. Electrical contact was established with large area Ag paste contacts, and four-point resistance measurements were conducted by applying a bias current I_0 and measuring the voltage V_m versus time t, with all being done at room temperature. The van der Pauw geometry with graphene constriction contacts was selected for scale invariant contact resistances R_{ci} (see Supporting Information) and a scale invariant four-point resistance R_{4pt}. To minimize the contribution of the metal-graphene junctions to the contact resistances R_{ci}, we employed a van der Pauw geometry with graphene constriction contacts. This allowed to use macroscopic mm-scale metal-graphene junctions for all van der Pauw sample of different L, allowing us to minimize the noise contribution of the metal-graphene junctions [98].

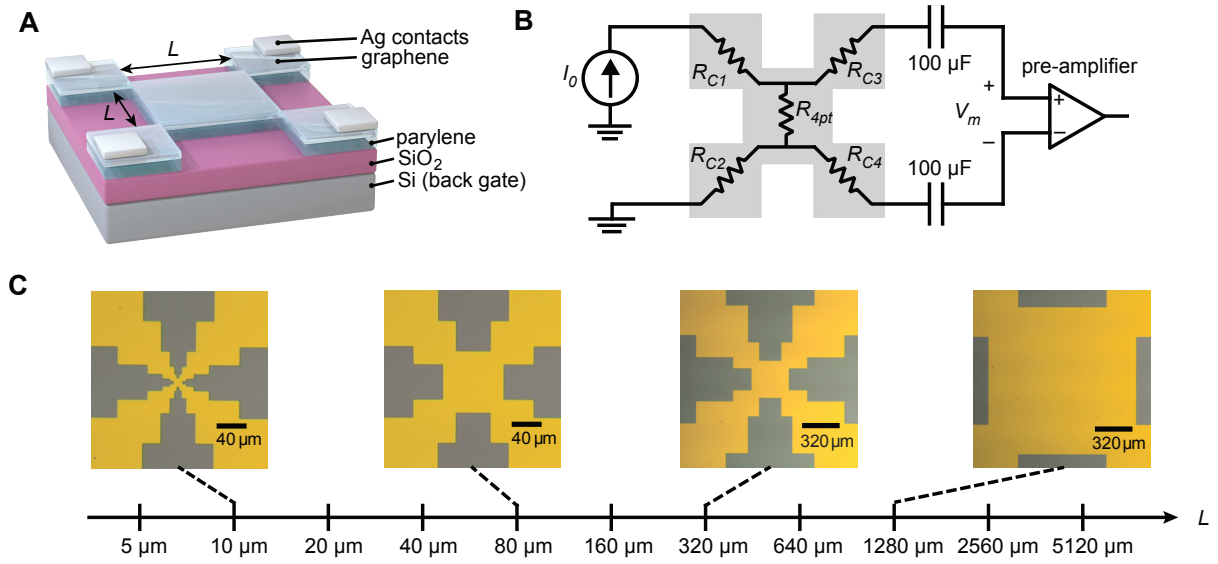

Figure 5.1: Graphene van der Pauw field effect transistors. **A** Illustration of graphene van der Pauw FET structures, where the layers are (bottom to top) n-Si, 300nm SiO_2, 130nm parylene C, graphene, Ag electrical contacts. **B** Circuit diagram of our 4-point voltage noise measurement apparatus. A current I_0 was applied across contacts 1 and 2 with the silicon back gate connected to the reference contact 2. The voltage V_m was measured across contacts 3 and 4, with the DC component filtered out using two 100 μF capacitors. **C** Optical images of representative van der Pauw FETs with lengths L of (left to right) 10 μm, 80 μm, 320 μm, and 1280 μm.

A representative set of measured V_m versus time t is shown in Fig. 5.2A at different bias graphene FET channel voltages $V_0 = I_0 R_{4pt}$ for the smallest graphene FET ($L^2 = 25$ μm^2) used in our study. The corresponding voltage PSD S_V versus frequency f calculated from the V_m time series (see Supporting Information) are shown in Fig. 5.2B, where it is observed that $S_V \propto 1/f$ and $S_V \propto V_0^2$. The background $1/f$ noise contributions from the amplifier and current source have a PSD $S_V = 3 \times 10^{-14}$ V^{2}Hz^{-1} at $f = 1$ Hz. For each graphene FET,

the normalized $1/f$ noise parameter $K = S_V f/V_0^2$ was determined with an experimental uncertainy of 6.1%. According to Hooge's empirical scaling law, the noise parameter,

$$K = \frac{\alpha_H}{N} = \frac{\alpha_H}{nL^2}. \tag{5.2}$$

Hall measurements were used to determine the charge carrier density n (see Supporting Information). All graphene FETs were found to be p-type at zero gate voltage bias. The mean and standard deviation in charge carrier density evaluated over all van der Pauw devices are $\langle n \rangle = 9.0 \times 10^{12}$ cm^{-2} and $\sqrt{\langle \Delta n^2 \rangle} = 8.5 \times 10^{-11}$ cm^{-2} respectively, while the mean and standard deviation in mobility are $\langle \mu \rangle = 1700$ cm^{2}V^{-1}s^{-1} and $\sqrt{\langle \Delta \mu^2 \rangle} = 240$ cm^{2}V^{-1}s^{-1} respectively. We can thus see that there is negligible variation in both the charge carrier density and mobility of all our devices across more than 6 orders of magnitude variation in area. The measured K versus charge number $N = nL^2$ is shown in Fig. 5.2C, where it can be observed that there is a notable variation in the Hooge parameter from device to device ($0.061 < \alpha_H < 1.20$). The variation in Hooge parameter among graphene FETs is in accord with the observation that *extrinsic* factors such as charge trap density contributes to $1/f$ noise [33, 96]. From a linear fit of K versus N in the log domain, we find a mean Hooge parameter $\alpha_H = 0.34$.

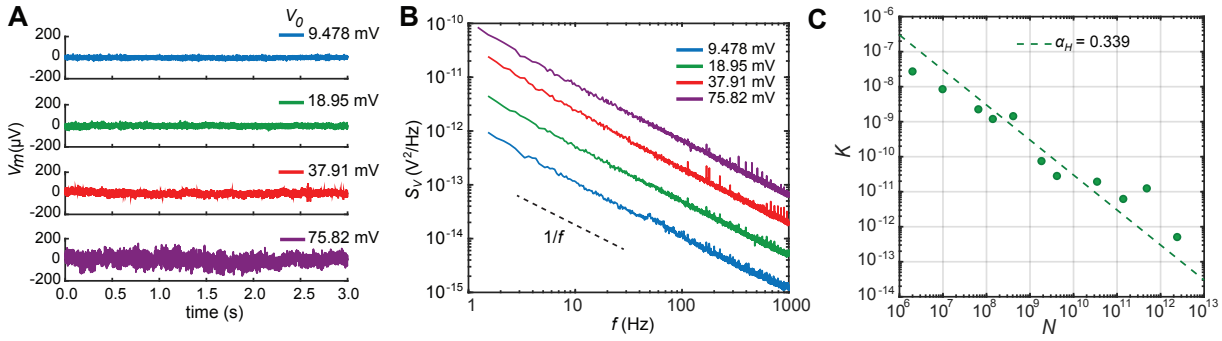

Figure 5.2: Noise measurements. A Measured voltage V_m versus time t of a $L = 5$ μm van der Pauw FET with varrying dc bias I_0. The measured 4-point dc voltage $V_0 = I_0 R_{4pt}$ is shown. **B** Corresponding voltage power spectral density S_V of the $L = 5$ μm van der Pauw FET versus frequency f with corresponding dc voltage V_0. Noise increases quadratically with dc bias. **C** Noise parameter, K of all van der Pauw FETs plotted versus the measured charge carrier number N. The linear best-fit of K versus N to an empirical Hooge model gives a Hooge parameter $\alpha_H = 0.339$

We consider now the implications of graphene FET size on sensor signal to noise ratio. For simplicity, we consider a graphene FET sensor where a sensing event translates to a modulation in surface potential $\delta\phi$ and in turn to a modulation $\delta V_m = I_0 \delta R_{4pt}$ in graphene FET channel potential. Our analysis can be readily generalized to other physical mechanisms that produce a modulation in graphene FET channel potential. The voltage noise power P_N over an electrical bandwidth $f_1 \leq f \leq f_2$,

$$P_N = \frac{1}{R_{4pt}} \int_{f_1}^{f_2} S_V df = \frac{K V_0^2}{R_{4pt}} \ln\left(\frac{f_2}{f_1}\right), \tag{5.3}$$

and the signal power,

$$P_S = \frac{1}{R_{4pt}} \left(\frac{\partial V_m}{\partial \phi} \delta\phi \right)^2, \tag{5.4}$$

with the SNR $= P_S/P_N$ consequently,

$$\text{SNR} = \frac{\beta^2}{K} \frac{\delta\phi^2}{\ln(f_2/f_1)}, \tag{5.5}$$

where β is the normalized FET gain referenced to the surface potential,

$$\beta = \frac{1}{R_{4pt}} \frac{\partial R_{4pt}}{\partial \phi}. \tag{5.6}$$

The SNR thus depends upon the normalized gain β and the normalized noise parameter K. The gain $\beta = \mu C_q \rho$ in a simple Drude conductivity model with mobility μ, quantum capacitance $C_q = e\partial n/\partial\phi$, and $\rho = (ne\mu)^{-1}$ is the sheet resistivity. For a fixed channel aspect ratio such as the square used in our work, the gain β is independent of absolute graphene size L, with the caveat that L is larger than absolute length scales such as mean-free path or Fermi wavelength. In contrast to this scale invariant behaviour, the noise parameter $K \propto 1/L^2$. Improved SNR can thus be achieved by scaling a graphene FET *larger*.

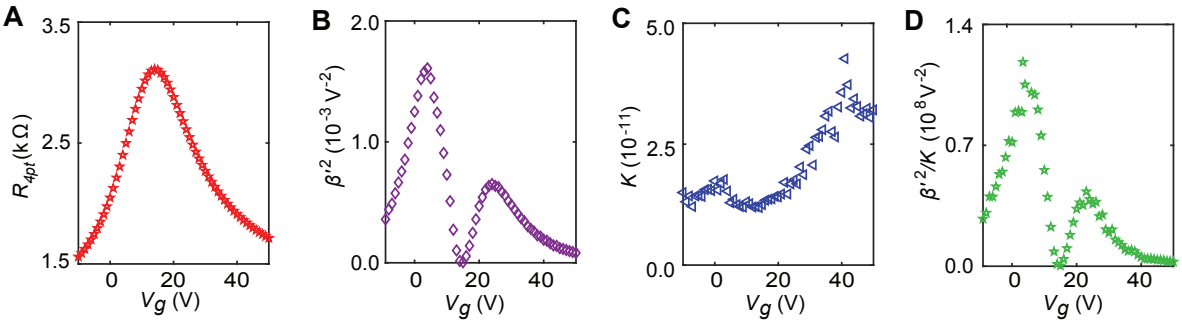

Figure 5.3: Graphene transistor parameters. **A** The 4-point resistance R_{4pt} of a $L = 640$ μm graphene van der Pauw FET versus back gate voltage V_g. **B** β'^2 of the corresponding 640 μm device versus back gate voltage V_g, showing strong modulation. **C** Noise parameter, K, measured using the 4-point noise measurement method of the corresponding 640 μm device versus the back gate voltage V_g. Modest modulation is observed. **D** FET SNR parameter, β'^2/K, of the corresponding 640 μm device versus the back gate voltage V_g, where the gate voltage dependence is dominated by gate modulation of β'^2.

The gain β remains an important parameter in determining graphene FET sensor SNR. The four-point resistance R_{4pt} versus back-gate voltage V_g for a graphene FET with $L = 640$ μm and back-gate capacitance $C_g = 7.5$ nFcm^{-2} is shown in Fig. 5.3A. The gain $\beta' = \partial \ln R_{4pt}/\partial V_g = (C_g/C_q) \cdot \beta$ referenced to the back-gate voltage can be directly determined from R_{4pt} versus back-gate voltage V_g. Fig. 5.3B shows the parameter β'^2 versus gate voltage V_g, where it is seen that β'^2 is strongly modulated by gate voltage V_g, with a null appearing at the charge neutrality point $V_g = 14$ V where $\partial R_{4pt}/\partial V_g = 0$, and local maxima appear for both electron and hole conduction. The measured noise parameter K and SNR factor β'^2/K are shown in Figs. 3C and D, respectively. The noise parameter K shows only modest variation of less than an order of magnitude over the same range of gate voltage

V_g, including non-monotonic behaviour around neutrality as has frequently been observed in graphene FETs [36, 96, 97]. Gate-voltage tuning of the graphene FET SNR parameter β'^2/K thus primarily occurs through the modulation of gain β'^2 rather than the noise K.

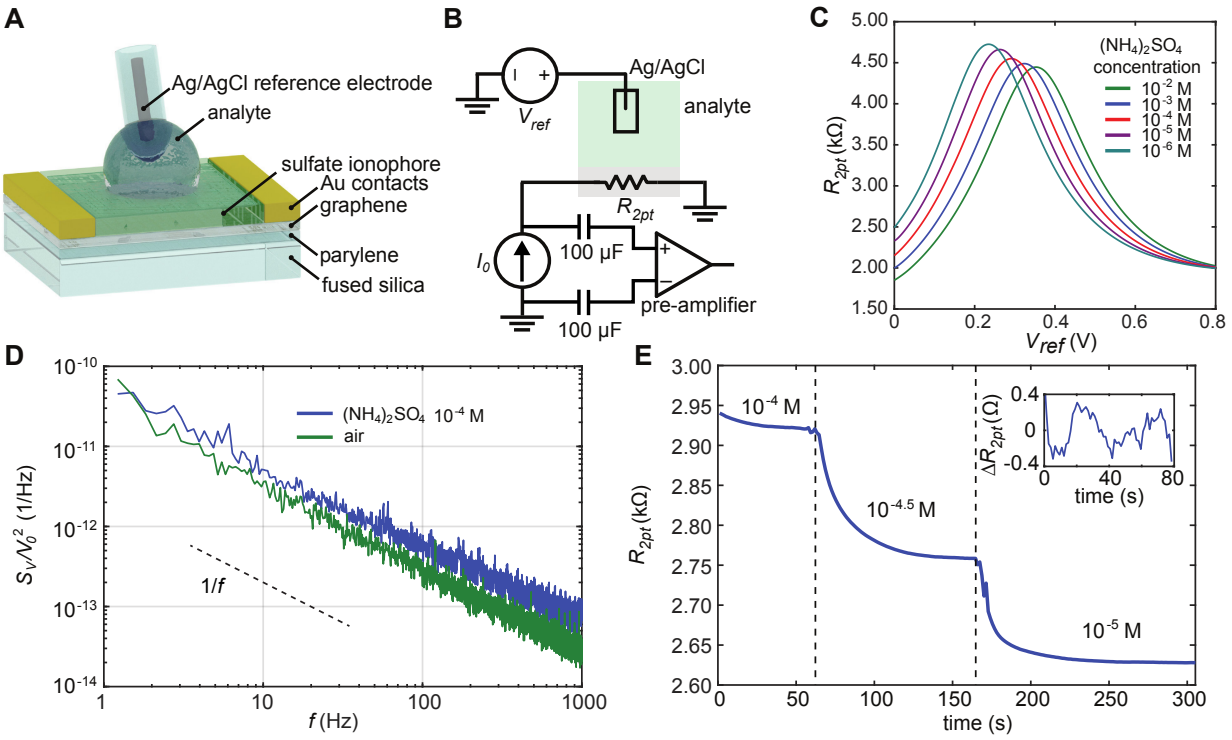

Figure 5.4: Graphene sulfate sensor. **A** Illustration of our GFET sulfate sensor, where the layers are (bottom-top) fused silica, 130nm parylene C, graphene, au contants and sulfate ionophore. **B** Circuit diagram of the noise measurement system with the gate voltage V_{ref} applied through the Ag/AgCl electrode and analyte. **C** The 2-point resistance, R_{2pt} plotted against the gate reference voltage V_{ref} at the various concentrations. **D** The normalized voltage power spectral density S_V/V_0^2 at a dc bias current of $I_0 = 1$ mA with $V_{ref} = 0$V in both dry (air) and wet (10^{-4}M ammonium sulfate) conditions. **E** The 2-point resistance, R_{2pt}, of the graphene sulfate sensor measured in real time as ammonium sulfate concentration is spiked. The inset shows the residual resistance fluctuation at 10^{-5}M ammonium sulfate, revealed by subtraction of the transient (exponential decay) signal in response to sulfate concentration spiking.

As a representative example of a large-area, low-noise sensor, we consider a graphene ISFET designed for sensing sulfate ions. The graphene ISFET is in a two-point geometry

with a square active area of size $L = 10$ mm, the graphene is supported on a parylene/fused silica substrate, and is non-covalently functionalized with an ionophore membrane (see Supporting Information). Measurements were conducted with a Ag/AgCl reference electrode, as shown schematically in Fig. 5.4A. The two-point resistance $R = V_0/I_0$ versus reference potential V_{ref} with different concentrations of the sulfate ion analyte is shown in Fig. 5.4B, from which it was inferred that the surface potential shifts by approximately 29.4 mV per decade $(NH_4)_2SO_4$ molar concentration, this is the limit defined by the Nernst equation for divalent ions at room temperature. The voltage PSD S_V of the graphene channel voltage was measured using the 2 point measurement technique by measuring the drain source voltage, while applying a current bias of 1 mA in dry (air) and wet conditions is shown in Fig. 5.4D, across the bias with the $V_{ref} = 0$ V. The noise in the wet condition is approximately 3-4 times larger in noise power compared to the dry condition, we believe this is due an increase in amplitude of charge fluctuations. A typical time dependent measurement of graphene ISFET resistance R versus time t as sulfate ion concentration is spiked is shown in Fig. 5.4E, with an electrical bandwidth 0.003 Hz $< f <$ 0.5 Hz. The inset of Fig. 5.4E shows the measured resistance fluctuation ΔR about the exponential resistance signal (see Supporting Information). The limit of detection of our sulfate sensor is below 1×10^{-5} M. The standard deviation of the resistance was measured to be $\sqrt{\langle \Delta R^2 \rangle} = 120$ mΩ. With a measured resistance sensitivity of $s = 295$ Ω/log(M), we observe a sulfate ion resolution of $r = 1.2 \times 10^{-3}$ log(M) at $k = 3$ confidence factor. The

resolution of our graphene ISFET is more than 16 times improved over that of state of the art silicon ISFETs targetting monovalent species [57], and more than 80 times improved over that of reported sulfate ISFETs [100]. We further find that our graphene ISFET has a resolution 4 times improved over the low-noise bipolar junction/field effect hybrid ion sensor, which is the lowest noise silicon based ion sensor reported to date [101].

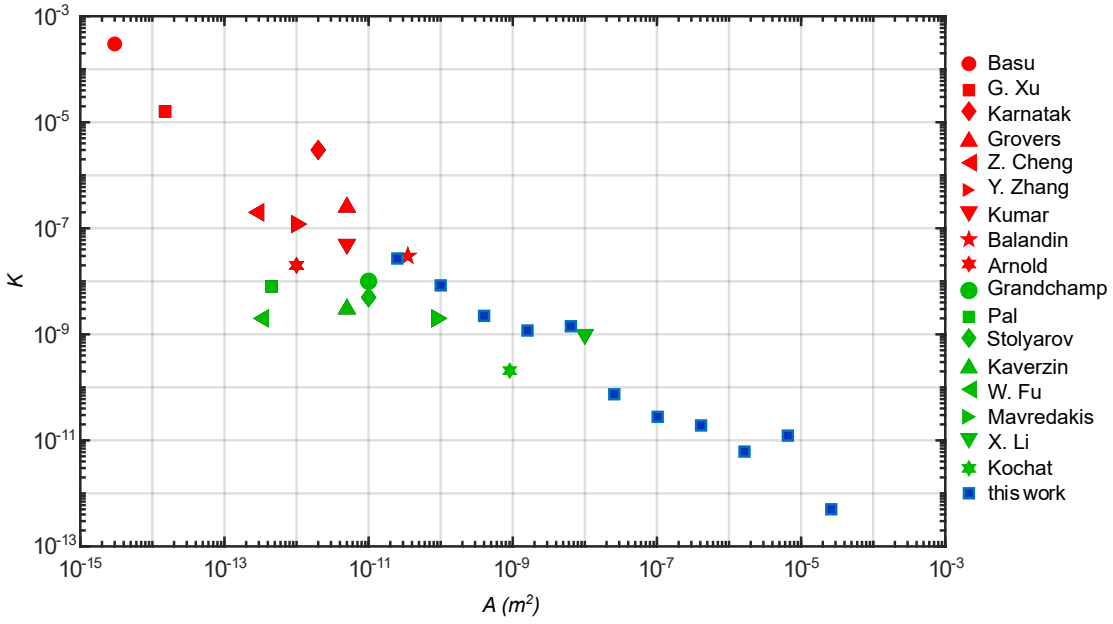

Figure 5.5: Noise comparison. A summary of the noise parameter, K versus GFET area, A. The noise parameter for this work (blue symbols), reaching $K = 5\times10^{-13}$ for $A = 26\,\mathrm{mm}^2$, is lower than that reported in previous works (red and green symbols), including that of Basu [102], G. Xu [96], Karnatak [98], Grover [103], Cheng [104], Zhang [97], Kumar [105], Balandin [36], Arnold [106], Grandchamp [107], Pal [95], Stolyarov [24], Kaverzin [23], W. Fu [87], Mavredakis [108], X. Li [109] and Kochat [110]. The overall trend is evident, wherein K decreases as GFET area A increases, in accord with Hooge's empirical model.

Finally, we compare the room temperature $1/f$ noise parameter K versus graphene FET area $A = WL$ as reported in our work and previously reported works in Fig. 5.5. Despite the variation amongst graphene FETs of comparable size, the evident trend is that of lower noise parameter K for larger area graphene FETs. Note that the noise comparison of Fig. 5.5 includes measurements of a diversity of graphene FETs, including graphene prepared by mechanical exfoliation and CVD synthesis and transfer, a variety of substrate materials, a variety of FET geometries and a variety of contact electrodes. Nonetheless, the overall trend is in accord with Hooge's empirical observation $K = \alpha_H/nA$, where both n and α_H vary amongst graphene FETs. The graphene FETs studied in this work have the lowest K reported to date due to their large physical size.

5.3 Conclusion

In conclusion, we find that the absolute physical scale of a graphene FET is an important and thus far overlooked parameter that determines graphene FET sensor resolution. The advent of wafer-scale graphene synthesis and transfer methods [19,111–113] enables facile fabrication of large area graphene FETs. As Moore noted [114], transistor size for a particular application is determined by the economic trade-off between the cost of manufacturing and the value of circuit function. Our work shows that scaling FETs to *larger* dimensions is advantageous for reducing low-frequency noise and improving sensor resolution, in marked contrast with the advantageous scaling of FETs to *smaller* dimensions for digital electronics. In other

words, sensing applications may favour low-noise and low-bandwidth functionality, while computational applications favour high-density and high-bandwidth functionality. While the $1/A$ scaling of $1/f$ noise is expected to apply to all FETs, we note that our findings are particularly salient for graphene based FETs due to the comparatively simple fabrication methods available for synthesis of large-area graphene FETs as compared to conventional semiconductors.

Chapter 6

Solid Reservoir Reference Electrode

In the preceding chapter, we focused on quantifying the fluctuations and uncertainties of thermoelectric and graphene FET sensors. In this chapter, we address the design and development of reference electrodes for optimal electrochemical potential stability. The temporal electrochemical potential stability of the reference electrode is crucial for achieving accurate and precise measurement of ion concentrations in potentiometric-based sensors and for measuring bio-signals such as electroencephalogram (EEG) and electrocardiogram (ECG). We introduce a novel reference electrode, the solid reservoir reference electrode (SRRE), designed to replace traditional liquid-filled Ag/AgCl reference electrodes in certain applications by eliminating the need for wet storage and extending shelf life. The SRRE is constructed with a layer of Ag/AgCl paint, a solid KCl reservoir, and a porous polydimethylsiloxane (PDMS) membrane. This configuration ensures stable

electrochemical potential and long-term drift characteristics comparable to those of conventional Ag/AgCl electrodes. The SRRE demonstrates robust performance across both aqueous and non-aqueous solvents, including acetonitrile, and integrates easily with graphene ion-sensitive field-effect transistors (ISFETs) for concurrent pH and Na^+ ion concentration measurements on a single chip. Furthermore, the SRRE exhibits exceptional efficacy in bioelectrode applications, enhancing signal quality for electrocardiogram (ECG) and electroencephalogram (EEG) recordings.[1]

6.1 Introduction

A reference electrode's primary role is to stabilize the potential between a metallic conductor with electrons as charge carriers and an electrolytic conductor with ions as charge carriers. They are used in practically every electrochemical measurement, including potentiometry, voltammetry, amperometry, and impedance spectroscopy. Ever since the first standard hydrogen electrode (SHE) was invented by Max Le Blanc [45], we have seen a gradual decrease in complexity and improved usability. Unlike the SHE of the past, the modern AgCl reference electrode does not require hydrogen gas or highly acidic solutions to operate. However, the liquid-filled AgCl reference electrode of today still requires wet storage in an aqueous KCl solution. Removing the wet storage requirement is the next step in improving its usability and allowing for it to be adapted in more applications, such as

[1]This chapter is based on a manuscript in preparation for submission.

potentiometric sensing in medical applications at point of care or field measurements without the need for a highly trained technician.

In this work, we report a solid reservoir reference electrode (SRRE) that achieves the performance of traditional immersed wire Ag/AgCl reference electrodes (REs) in a compact, layered structure. The SRRE is a solid, layered analogue of the Ag/AgCl RE, with a chlorinated silver film as the metallic electrode, a solid KCl layer serving as a saturated reservoir of chloride, and a porous polydimethylsiloxane (PDMS) layer acting as a membrane for the exchange of water and ions. In its current design, the SRRE requires a conditioning period of 4 hours in saturated aqueous KCl before a stable open circuit potential is observed. The characteristics of the SRRE, including impedance, noise, and long-term drift, can be tuned by adjustment of the PDMS membrane permeance and KCl solid reservoir size.

We have demonstrated the temporal stability of the RE open circuit potential (OCP), with drift less than 0.37 mV over 17 hours in deionized water. When compared against bare chlorinated silver, the SRRE exhibits superior stability of OCP versus changes in electrolyte ion concentration, including solutions of potassium chloride, sodium chloride, and pH buffers. In addition, we demonstrate the SRRE's suitability to be used in non-aqueous environments such as acetonitrile, with a potential drift, monitoring the ferrocene/ferrocenium reaction in acetonitrile of less than 3 mV over a period of 8 hours. The ease of fabrication enables SRRE integration with graphene ion-sensitive field-effect

transistors (ISFETs) to achieve entirely solid-contact micro ion sensors. The solid-contact micro ion sensor can simultaneously measure pH and Na^+ on a single chip. Using the same layered structure, we further demonstrated electrocardiogram (ECG) and electroencephalogram (EEG) measurement with significantly lower impedance and noise compared to conventional gel electrodes.

6.2 Theory

The Ag/AgCl RE is the most widely used RE in aqueous solvents. At the heart of the Ag/AgCl RE is the redox reaction between the Ag, AgCl, and Cl^-(aq), where,

$$AgCl(s) + e^- \leftrightarrows Ag(s) + Cl^-(aq), \tag{6.1}$$

allowing for efficient electron to ion charge transfer. The commercially available and conventional Ag/AgCl RE consist of a glass structure containing a chlorinated Ag wire immersed in a highly concentrated (1-3 M) aqeuous KCl solution, terminated with a porous frit. The latter is immersed into the electrolyte of interest, allowing KCl to establish an equipotential with the surrounding aqueous electrolyte by ionic conduction. The requirement for ionic conduction also allows for KCl to leak from the finite reservoir within the electrode through the frit. As can be inferred from the redox reaction (Eq. (6.1)), the electrode potential is dependent upon the Cl^-(aq) concentration in the

reservoir. A stable RE thus requires a stable Cl^-(aq) concentration within the reservoir.

The structure of the SRRE is shown in Fig. 6.1A, where the porous glass frit is substituted by a thin layer of porous polydimethylsiloxane (PDMS), the reservoir of KCl is replaced by solid ball-milled KCl powder, and the chlorinated Ag wire is replaced by Ag/AgCl paint. Due to KCl's high solubility and hygroscopic nature, when the SRRE is exposed to water, water moves through the porous PDMS and into the powder KCl, forming ionic conduction channels. This allows for the establishment of an equipotential with the environment while locally saturating the concentration of chloride near the AgCl layer. The porous PDMS functions in the SRRE similarly to how the frit would in the conventional Ag/AgCl RE, which is to slow down the diffusion of K^+ and Cl^- ions while still allowing for ionic conduction between the outer environment and the inside of the RE.

The scanning electron microscope image of the porous PDMS layer created using the KCl-infused method is shown in Fig. 6.1B. To fabricate the porous PDMS, the KCl-infusion method was employed, wherein ball-milled KCl powder was mixed with the PDMS precursor. After curing the PDMS, the entire structure was exposed to water, rapidly dissolving the solid KCl inside, leaving behind a porous PDMS structure. This process is illustrated in Fig. 6.1C. Fig. 6.1D presents an optical image of the SRRE after the deposition of the Ag/AgCl paint layer, ball-milled KCl layer, and the porous PDMS layer.

The absence of water in the entire structure of the SRRE after fabrication allows for a significantly longer shelf life compared to conventional Ag/AgCl REs. The layered structure

of the SRRE enables planar processing.

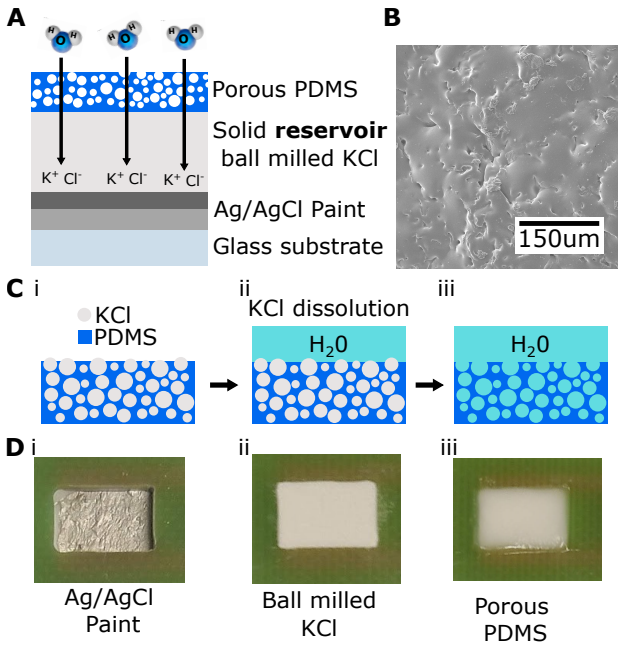

Figure 6.1: Fabrication and structure. **A** Cross sectional structure diagram of the solid reservoir reference electrode, showing the layered structure of the Ag/AgCl paint, balled milled KCl and the top porous PDMS layer. **B** Scanning electron microscope image of the porous PDMS layer that was made using the KCL infused method. **C** Illustrative diagram of how porous PDMS is made using the KCL infused method. PDMS precursor is mixed with ball milled KCL powder, and left to cure. The structure becomes proous after dissolution of KCl powder in water. **D** Optical images of the solid reservoir reference electrode after the deposition of Ag/AgCl paint, ball milled KCl powder and porous PDMS layer.

6.3 Methods and results

Reagents

KCl, Sylgard 184 (PDMS), NaCl, pH buffers, Ag/AgCl (60/40) paste, Tetrabutylammonium hexafluorophosphate ($TBAPF_6$) 98%, Pt wire 99.9%, graphite electrodes 99.9%, deionized water > 2.3 MΩcm, ferrocene > 98%, hydrogen ionophore II (ETH 1907), sodium ionophore X, high molecular weight polyvinyl chloride (PVC), dioctyl sebacate (DOS), cyclohexanone, and potassium tetrakis(4-chlorophenyl)borate were all purchased from Sigma-Aldrich Canada. Fused silica wafers were purchased from University Wafer. Low-temperature solder paste (Sn42Bi57Ag1) was purchased from MG Chemicals. SU-8 2002 was purchased from MicroChem. Disposable bioelectrodes were purchased from Tianrun Medical.

Fabrication of solid reservoir reference electrode

Ag/AgCl paint was coated on a glass substrate and attached to a printed circuit board with a center cavity, as can be seen in Fig. 6.1D i. Ball-milled KCl powder was packed into the cavity, occupying a depth of 1.6 mm, as can be seen in Fig. 6.1D ii. To coat the final top layer, Sylgard 184 precursor A and B were mixed at the recommended 10:1 ratio. The precursor mixture was combined with ball-milled KCl using a pick at a mass ratio of 1:1 until the final mixture appeared homogeneous. The combined mixture of precursor and KCl

was deposited with the thickness being controlled using a doctor blade to 300 μm onto the electrode, as can be seen in Fig. 6.1D iii.

Fabrication of ion sensitive field effect transistor

Fused silica wafers, 100 mm wide and 0.5 mm thick, were coated with 300 nm of Parylene C and monolayer graphene grown by chemical vapour deposition was transferred (Graphenea). After the graphene was transferred onto the substrate, 100 nm thick gold (Au) contacts were evaporated onto the wafer with the aid of photolithography to form source and drain contacts. Reactive ion etching was employed to remove the unwanted graphene, and SU-8 was used to passivate the exposed metal contacts. The graphene FETs were then mounted onto the PCB using the flip-chip method with low-temperature solder paste.

To make the graphene FET sensitive to Na^+ ions and H^+ ions, PVC-based cocktails with sodium ionophore and hydrogen ionophore were deposited, respectively and left to dry overnight.

The sodium ionophore PVC-based cocktail contains 330 mg PVC, 660 mg DOS, 24 mg sodium ionophore X, 10 mg potassium tetrakis(4-chlorophenyl)borate, and 4 mL cyclohexanone. The hydrogen ionophore PVC-based cocktail contains 330 mg PVC, 660 mg DOS, 24 mg hydrogen ionophore II, 10 mg potassium tetrakis(4-chlorophenyl)borate, and 4 mL cyclohexanone.

Fabrication of SRRE bioelectrode

The bioelectrodes were made by first removing the top gel layer of the disposable electrodes. Ag/AgCl was painted on top of the exposed metal, and a thin layer of approximately 0.5 mm of powdered KCl was applied to the Ag/AgCl paint layer. To coat the final top layer, Sylgard 184 precursor A and B were mixed at the recommended 10:1 ratio. The precursor mixture was combined with ball-milled KCl using a pick at a mass ratio of 1:1 until the final mixture appeared homogeneous. The combined mixture of precursor and KCl was deposited with the thickness being controlled using a doctor blade to 300 μm onto the electrode. The electrode was left to cure over 24 hours at room temperature. The electrode was conditioned in 1 M KCl before being used.

Open circuit potential measurements

All OCP measurements of the SRRE were performed against a conventional Ag/AgCl (3M KCl) reference electrode (BASi MF-2056), using a PalmSens 4 potentiostat. The sampling rate was 1 sample per second.

Impedance spectroscopy

Impedance spectroscopy was conducted using a lock-in amplifier (Zurich Instruments MFLI 500 kHz) and a current source (Stanford Research Systems CS580), with a Pt wire as the counter electrode and an Ag/AgCl (3M KCl) electrode as the reference. For measurements

on the SRRE (working electrode), a current of $i = 1\,\mu$A was applied across frequencies from 1 Hz to 10 kHz using the current source between the working and counter electrodes. The lock-in amplifier measured the voltage V between the working and reference electrodes, and impedance Z was then calculated by $Z = V/i$.

Cyclic voltammetry of ferrocene

Cyclic voltammetry was performed using the Palmsens 4 potentiostat in acetonitrile, using a glass container with 1 mM ferrocene and 0.1 M $TBAPF_6$ as the supporting electrolyte, using a graphite working electrode, a graphite counter electrode, and the SRRE as the reference electrode. The voltage was swept from 0 V to 0.8 V at a rate of 1 mV per second.

Graphene ion sensitive field effect transistor measurements

All graphene ISFET-related measurements were performed using a semiconductor device parameter analyzer (Agilent Technology B1500A). The SRRE was used as the RE in the system. A fixed voltage bias of 100 mV was applied between the drain and source of each graphene FET. While measuring the drain-source current I_{ds}, the voltage between the reference electrode and the source, V_{ref} was swept from -300 mV to 600 mV at a rate of 50 mV per second.

Biosignal measurements

The lead I ECG signal of the author, Tran, was measured between the left wrist and the right wrist, while the EEG signal was measured between the forehead and the back of the ear. The biosignals were amplified using the DFRobot SEN0123 preamplifier and digitized using the analog-to-digital converter (DT-9847) from Data Translation. To measure the impedance across Tran's forearm at a distance of 58 mm, a current source (Stanford Research Systems CS580) was used to apply a current of i= 1 μA, between 10 Hz and 10 kHz. The voltage V was measured using a lock-in amplifier (Zurich Instruments MFLI 500 kHz). The impedance Z=V/i.

Results and discussion

A good RE is characterized by a stable electrochemical potential that is independent of ion concentration and is stable throughout time. To demonstrate the stability of our SRRE, we measured the SRRE's OCP, plotted in blue in Fig. 6.2A, while comparing it against a commonly used type of RE in screen-printed sensors, a bare planar AgCl reference electrode, plotted in a dashed green line in Fig. 6.2A. We measured the OCP of the SRRE and the bare AgCl RE in solutions of pH buffers (Fig. 6.2Ai), aqueous KCl (Fig. 6.2Aii), and aqueous NaCl (Fig. 6.2Aiii). We find there is significant drift in the bare AgCl RE in the pH buffer solution, up to 50 mV per minute, where no Cl^- ions are present, while in solutions of NaCl and KCl, the potential of the plain AgCl RE varies up to 50 mV/decade

of Cl^- ion concentration. In contrast, due to the solid reservoir of KCl, which stabilizes the concentration of Cl^- ions in the SRRE, the SRRE potential varies by less than 3 mV over multiple decades of changes in ion concentration.

To assess the temporal stability of the SRRE, the OCP of the SRRE was measured in the analyte that withdraws Cl^- ions from the RE at the maximum rate, deionized water, over a period of 15 hours, as can be seen in Fig. 6.2B. We find excellent electrochemical temporal stability of the SRRE with a drift of less than 0.37 mV over a span of 15 hours. Measuring the impedance of the SRRE over a frequency range from 1 Hz to 10 kHz, with the Nyquist plot shown in Fig. 6.2C, we estimate the DC resistance of the SRRE to be 35 kΩ, which is on par with other solid contact reference electrodes [115].

Conventional Ag/AgCl REs are not often used in non-aqueous solvents such as acetonitrile due to the clogging of the frit [116]. As the KCl moves from an aqueous environment with high KCl solubility to acetonitrile with low KCl solubility, the KCl often crystallizes and clogs the frit. Since the SRRE has no water to begin with, recrystallization and clogging is mitigated. To assess the SRRE stability in acetonitrile, we performed cyclic voltammetry in a 1 mM solution of ferrocene with 0.1M TBAPF6 as supporting electrolyte in acetonitrile, with a graphite counter electrode and graphite working electrode, where the redox reaction of ferrocene,

$$\mathrm{Fe(C_5H_2)_2} \leftrightarrows \mathrm{Fe(C_5H_2)_2^+} + e^- \tag{6.2}$$

was observed. The 2nd cyclic voltammogram is shown in Fig. 6.2D. As the ferrocene/ferrocenium is a stable redox couple [117, 118], we expect any change in the average of the reduction peak potential and oxidation peak potential to be due to the SRRE. Fig. 6.2E shows the average between the reduction peak potential and oxidation peak potential, E'_o as a function of time throughout the cycles of cyclic voltammetry. We find this electrochemical potential varies less than 3 mV over a period of 8 hours. The value of E'_o was found to be 448 ± 1.5 mV, which is in strong agreement with other published work [118], demonstrating that the SRRE is a suitable reference electrode in non-aqueous solvents such as acetonitrile.

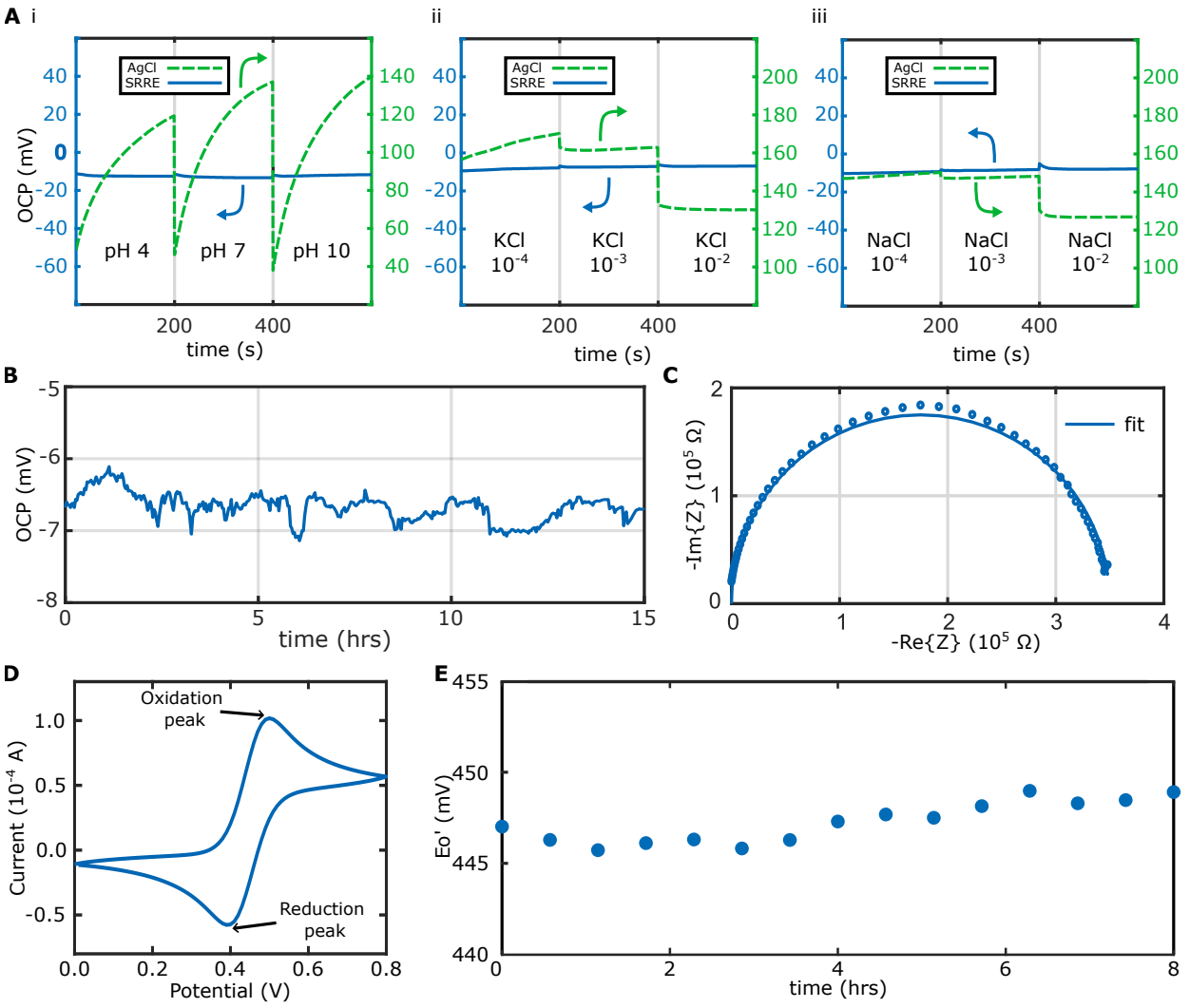

Figure 6.2: Solid reservoir reference electrode performance. **A** Open circuit potential of the SRRE (solid blue) and the plain AgCl RE (dashed green) measured against a standard AgCl RE (3M KCl) in solutions of pH buffers (i), aqueous KCl (ii), and aqueous NaCl (iii). **B** Drift analysis by measuring the open circuit potential of the SRRE against a standard AgCl RE (3M KCl) in deionized water over 15 hours. **C** Nyquist plot of the SRRE's impedance in a saturated aqueous KCl solution. The raw data points are shown as circles, while the fit is shown as a solid line. **D** Cyclic voltammogram in a solution of 1 mM ferrocene in acetonitrile, with the SRRE as the RE, graphite counter electrode, and graphite working electrode, demonstrating the reduction peak at potential E_{red}, and oxidation peak at potential E_{ox} **E** Plot of $E'_o = (E_{red} + E_{ox})/2$ as a function of time, through the cycles of cyclic voltammetry.

To demonstrate the SRRE's ease of integration and packaging, we packaged 6 ISFETs (3 sensitive to Na^+ and 3 sensitive to H^+) and our SRRE onto a single printed circuit board, as can be seen in Fig. 6.3A. We measured the neutrality point of the graphene ISFETs by sweeping the voltage of the SRRE, relative to the source contact, at a fixed drain-source bias voltage $V_{ds} = 100$ mV, while measuring I_{ds}, for pH ISFETs in pH buffers can be seen in Fig. 6.3B, with the extracted neutrality points shown in Fig. 6.3C. The I_{ds} of Na ISFETs in aqueous NaCl can be seen in Fig. 6.3D, with extracted neutrality points shown in Fig. 6.3E. Upon inspection of the neutrality point vs concentration, the voltage sensitivity can be determined to evaluate how close the sensor sensitivity is to the limit set by the Nernst equation, $\ln(10)\frac{k_B T}{en}$, where k_B, T, e, n, ln is the Boltzmann constant, temperature, charge of an electron, number valance electrons of the species and natural logarithm respectively. At room temperature the limit is 59.2 mV/decade for a monovalent ion species at room temperature. The voltage sensitivity for the H^+ was found to be 55.6 mV/decade, and Na^+ ISFETs were found to be 55.0 mV/decade.

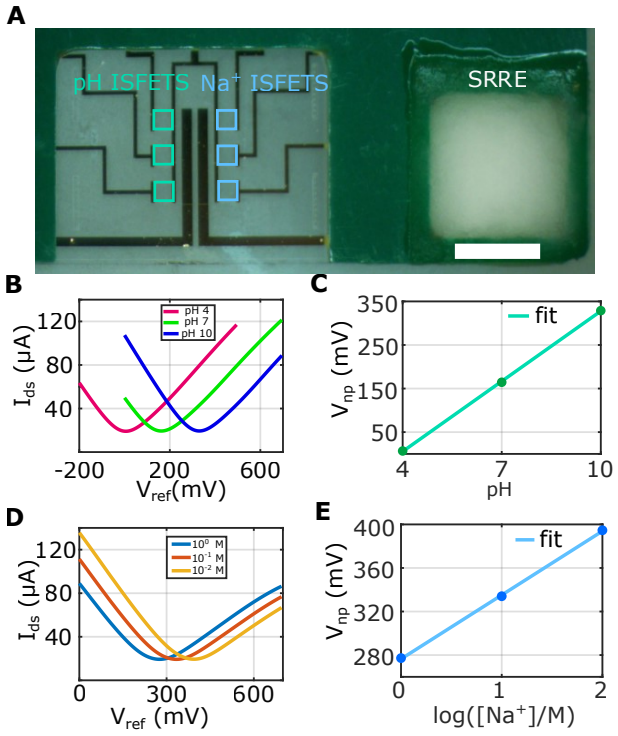

Figure 6.3: Integrated ISFETs with SRRE. A Optical image of the pH and Na^+ sensitive ISFETs with the SRRE on a single printed circuit board chip. The scalebar width is 3.5 mm **B** Plot of drain-source current I_{ds}, with a constant drain-source voltage bias of 100 mV, while sweeping the SRRE's voltage relative to the source, at different pH buffers for a pH-sensitive ISFET. **C** Plot of pH-sensitive graphene ISFET neutrality point V_{np} vs pH buffer concentration. The straight-line fit corresponds to a sensitivity of 55.6 mV/decade. **D** Plot of drain-source current I_{ds}, with a constant drain-source voltage bias of 100 mV, while sweeping the SRRE's voltage relative to the source, at different NaCl concentrations, for a Na^+ sensitive ISFET. **E** Plot of Na^+ sensitive graphene ISFET neutrality point V_{np} vs aqueous NaCl concentrations. The straight-line fit corresponds to a sensitivity of 55.0 mV/decade.

We evaluated the suitability of the SRRE to be used as a bioelectrode to measure the human body's ECG and EEG signals. As the human body is approximately 60% water,

ions are the main type of charge carrier present. In Figure 6.4B, the ECG signal of Tran was measured using both the SRRE (blue plot) and a disposable gel electrode (green plot). Upon close inspection of the ECG signals, the signal measured using the SRRE has less background noise, allowing for the Q-wave in the signal to be identified. In contrast, the Q-wave cannot be identified using the disposable gel electrode. The plot for the EEG signal in Figure 6.4C again shows that the signal measured using the SRRE has significantly less noise. Comparing the background EEG signal noise in Figure 6.4D, we find that the noise power is approximately 50% less when the SRRE is used instead of the disposable gel electrode. The reduction in noise is due to the low electrode-skin impedance of the SRRE. We demonstrated this by using the SRRE (blue plot) and disposable gel electrode (green plot) to measure the impedance across Tran's forearm over a distance of approximately 58 mm in Figure 6.4E. We find that the measured impedance is approximately one order of magnitude lower, at frequencies less than 100 Hz, when the SRRE is used in place of the gel electrode.

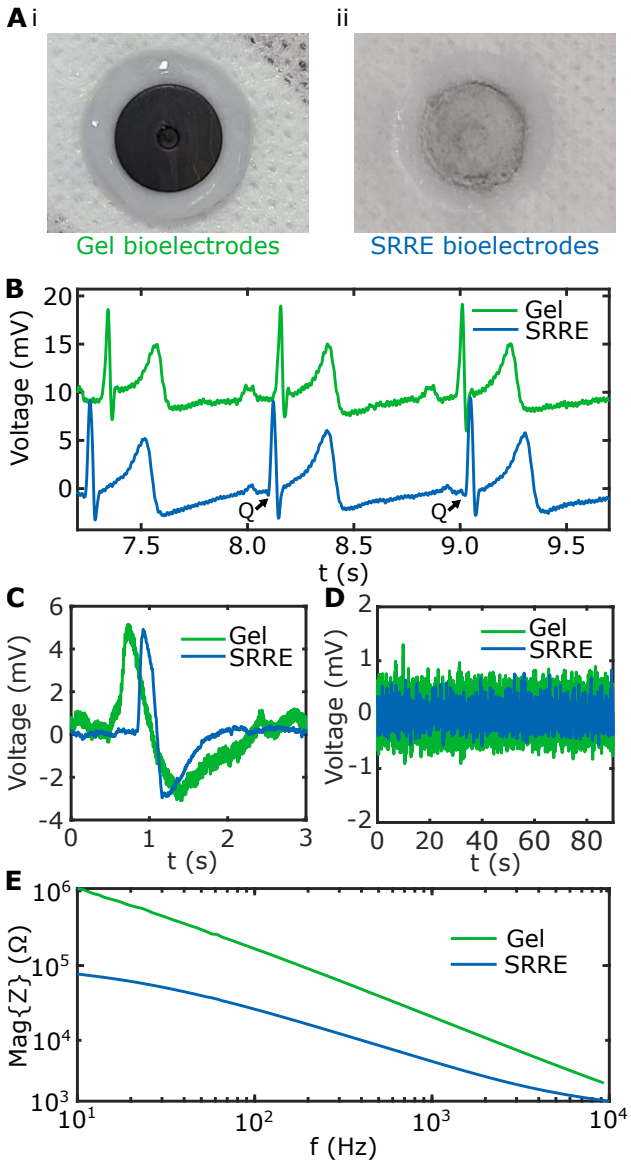

Figure 6.4: SRRE ECG and EEG electrodes. **A** i. Optical image of a disposable gel bioelectrode. ii. Optical image of the SRRE bioelectrode. **B** Lead I ECG signal measured across the left and right forearms using either the gel bioelectrode (green) or the SRRE bioelectrode (blue). The visible Q-wave of the ECG signal measured using the SRRE bioelectrode is highlighted. **C** EEG signal between the forehead and the back of the ear, recording an eye blink, using either a gel bioelectrode (green) or the SRRE bioelectrode (blue). **D** Background EEG signal between the forehead and the back of the ear, using either a gel bioelectrode (green) or the SRRE bioelectrode (blue). **E** Measured impedance of Tran's forearm across a distance of 58 mm using either a gel bioelectrode (green) or the SRRE bioelectrode (blue).

6.4 Conclusion

In conclusion, we introduced a reference electrode, the SRRE, that offers significant advantages over traditional Ag/AgCl reference electrodes. The SRRE achieves comparable performance in terms of stability, impedance, and noise, while eliminating the need for wet storage to extend shelf life. Our results demonstrated the SRRE's stable open circuit potential with minimal drift, excellent performance in both aqueous and non-aqueous environments, and ease of integration with ISFETs for miniaturized sensing applications.

The SRRE's layered structure, comprising a chlorinated silver film, a solid KCl layer, and a porous PDMS membrane, ensures consistent ionic conduction and stability. The fabrication method, involving the infusion of PDMS with ball-milled KCl, simplifies production and extends the electrode's shelf life. Our experiments highlighted the SRRE's suitability for various applications, including the measurement of ECG and EEG signals, where it exhibited lower noise and impedance compared to conventional gel electrodes.

Chapter 7

Conclusions, Discussion and Future Work

In this thesis, we have discussed a range of topics that, while seemingly disparate, are interconnected through their relevance to sensor technology. These topics include thermoelectric devices, graphene field-effect transistors, and electrochemical reference electrodes. Despite their different applications and mechanisms, a common theme emerges: the role of fundamental fluctuations and stability in determining the accuracy and precision of these sensor systems. By examining how these factors influence each type of sensor, we gain insight into how to potentially enhance their performance and reliability. Understanding these underlying principles is crucial for advancing sensor technology and improving measurement accuracy across various scientific and industrial applications.

In the first part of this thesis, we generalized the fluctuation-dissipation theorem to include thermoelectric materials and devices. We began by theoretically demonstrating the coupling between temperature fluctuations and voltage fluctuations in thermoelectric materials. Our findings indicated an enhanced voltage fluctuation spectral density of $4k_BTR(1+ZT)$ at frequencies below a thermal cut-off frequency f_T, where ZT represents the dimensionless thermoelectric device figure of merit. To validate our theoretical predictions, we experimentally measured this enhanced voltage power spectral density in an ultra-fast response ($f_T \sim 1$ kHz) integrated thermoelectric micro-device. By assessing the ZT-enhanced voltage noise, we resolved temperature fluctuations with an amplitude of 0.8 μK Hz$^{-1/2}$ at a mean temperature of 295 K. Our work establishes a quantitative understanding of temperature fluctuations in thermoelectrics, defining an important physical limit for micro-scale thermoelectric thermometry, such as intracellular thermometry [73]. Our work has proven relevant in various fields, including quantum confinement [119], where potential-temperature fluctuations significantly impact heat-current fluctuations in these systems. There is a growing interest in understanding the manipulation of heat and entropy within quantum-confined systems.

We note that our results can be generalized to other systems to measure fundamental fluctuations. One example is giant magnetoresistance materials, commonly found in hard disks [120], where one could potentially measure fundamental thermal fluctuations in magnetization. Another example is spin-orbit coupling, which can result in fundamental

excitations that carry both charge and spin. The correlated transport of charge and spin can, in principle, lead to a modification of the observable spectral density of voltage fluctuations. Moreover, the spectral density of voltage fluctuations may provide insight into the spectral density of spin fluctuations.

In the second part of the thesis, we reported a simple method for reducing $1/f$ noise in graphene based electrochemical sensors, by scaling the active area of graphene field effect transistor sensors. We measured $1/f$ noise in graphene field effect transistors that ranged in size from 5 μm $\times$ 5 μm to 5.12 mm $\times$ 5.12 mm, observing more than five orders of magnitude reduction in $1/f$ noise. We reported the lowest normalized graphene $1/f$ noise parameter observed to date, 5×10^{-13}, and demonstrated a sulfate ion sensor with a record resolution of 1.2×10^{-3} log molar concentration units. Our work highlighted the importance of area scaling in graphene field effect transistor sensor design, showing that increased channel area significantly improved sensor resolution.

While we have demonstrated methods to mitigate $1/f$ noise in graphene FETs, the discourse surrounding $1/f$ noise in graphene remains active. This noise may stem from the metal-graphene interface [98]. Potential origins of $1/f$ noise include mobility fluctuations [26], charge density fluctuations [121], or a confluence of both [122]. Additionally, the impact of impurities is under examination [123]. It will be intriguing to observe whether $1/f$ noise persists as the predominant noise source or even remains measurable in ultra-clean graphene [124] and ultra-high mobility graphene with Dirac

plasmas [125].

In the third part of the thesis, we presented the design and evaluated the performance of a component that is crucial for any electrochemical measurements, the reference electrode. Our solid reservoir reference electrode is designed to replace traditional liquid-filled Ag/AgCl reference electrodes in certain applications, by eliminating the need for wet storage and extending shelf life. The SRRE is constructed with a layer of Ag/AgCl paint, a solid KCl reservoir, and a porous PDMS membrane. The configuration ensures stable electrochemical potential and long-term drift characteristics comparable to those of conventional Ag/AgCl electrodes. The electrode demonstrates robust performance across both aqueous and non-aqueous solvents, including acetonitrile, and integrates easily with graphene ion sensitive field effect transistors for concurrent pH and Na^+ ion concentration measurements on a single chip. Furthermore, the electrode exhibits exceptional efficacy in bioelectrode applications, enhancing signal quality for electrocardiogram and electroencephalogram recordings.

Although we aimed to replace the traditional Ag/AgCl reference electrode, it will not be an easy task, as the traditional Ag/AgCl reference electrode had undergone decades of rigorous development. Its performance had been thoroughly tested, with its limits, use case scenarios, and maintenance procedures well understood. The same cannot be said about the SRRE. The SRRE would require further testing and validation for its intended applications, quantification of its lifetime, and understanding of its failure mechanisms for potential improvement.

On a more inquisitive note, while we have demonstrated a solid analog of the liquid-filled Ag/AgCl electrode, the potential for a solid analog to the liquid-filled ion selective electrode and its performance remains to be explored. Additionally, measuring noise in electrochemical systems, such as the chlorinated silver wire in KCl, is of interest to determine if $1/f$ or other types of noise are present in the open circuit potential. Electrochemical noise measurements have primarily focused on corrosion monitoring, emphasizing the detection of discrete changes in spectral density associated with pit formation [126]. Another point of interest is the reference electrode's adherence to the Ohmic Johnson-noise formula, as there could be a modification of the spectral density of fluctuations arising from the electrochemistry at the interface, similar to the breakdown of the Nernst-Einstein relation for ion transport through carbon nanotube porins [127]. Theoretical work to develop molecular-scale models of electrochemical noise is ongoing [128]. In summary, the nature of fluctuations in nanoscale electrochemical systems is not yet understood.

Bibliography

[1] MV Vedernikov and EK Iordanishvili. Af ioffe and origin of modern semiconductor thermoelectric energy conversion. In *Seventeenth International Conference on Thermoelectrics. Proceedings ICT98 (Cat. No. 98TH8365)*, pages 37–42. IEEE, 1998.

[2] Thomas Johann Seebeck and Arthur Oettingen. *Magnetische polarisation der metalle und erze durch temperatur-differenz*. Number 70. W. Engelmann, 1895.

[3] Stephen J Blundell and Katherine M Blundell. *Concepts in thermal physics*. Oup Oxford, 2010.

[4] Jean Charles Athanase Peltier. *Nouvelles expériences sur la caloricité des courans électriques*. 1834.

[5] William Thomson. Ix.—on the dynamical theory of heat. part v. thermo-electric currents. *Earth and Environmental Science Transactions of The Royal Society of Edinburgh*, 21(1):123–171, 1857.

[6] Aapo Varpula, Anton Murros, Kuura Sovanto, Arto Rantala, David Gomes Martins, Kirsi Tappura, Jonna Tiira, and Mika Prunnila. Uncooled nano-thermoelectric bolometers for infrared imaging and sensing. In *Optical Components and Materials XX*, volume 12417, pages 143–152. SPIE, 2023.

[7] Changling Wang, Ruizhi Xu, Wenjuan Tian, Xiaoli Jiang, Zhengyu Cui, Meng Wang, Huaming Sun, Kun Fang, and Ning Gu. Determining intracellular temperature at single-cell level by a novel thermocouple method. *Cell research*, 21(10):1517–1519, 2011.

[8] Zhi-Gang Chen, Guang Han, Lei Yang, Lina Cheng, and Jin Zou. Nanostructured thermoelectric materials: Current research and future challenge. *Progress in Natural Science: Materials International*, 22(6):535–549, 2012.

[9] Joya A Cooley, Phichit Promkhan, Shruba Gangopadhyay, Davide Donadio, Warren E Pickett, Brenden R Ortiz, Eric S Toberer, and Susan M Kauzlarich. High seebeck coefficient and unusually low thermal conductivity near ambient temperatures in layered compound yb2–x eu x cdsb2. *Chemistry of Materials*, 30(2):484–493, 2017.

[10] Xiaoqing Lu, Guilong Pan, Zhan Shi, Biao Xu, and Yue Lou. Recent advances in interface engineering of thermoelectric nanomaterials. *Materials Chemistry Frontiers*, 2023.

[11] Jing-Feng Li, Wei-Shu Liu, Li-Dong Zhao, and Min Zhou. High-performance nanostructured thermoelectric materials. *NPG Asia Materials*, 2(4):152–158, 2010.

[12] Harry Nyquist. Thermal agitation of electric charge in conductors. *Physical review*, 32(1):110, 1928.

[13] Herbert B Callen and Theodore A Welton. Irreversibility and generalized noise. *Physical Review*, 83(1):34, 1951.

[14] Crispin Gardiner and Peter Zoller. *Quantum noise: a handbook of Markovian and non-Markovian quantum stochastic methods with applications to quantum optics*. Springer Science & Business Media, 2004.

[15] Aashish A Clerk, Michel H Devoret, Steven M Girvin, Florian Marquardt, and Robert J Schoelkopf. Introduction to quantum noise, measurement, and amplification. *Reviews of Modern Physics*, 82(2):1155, 2010.

[16] Philip Richard Wallace. The band theory of graphite. *Physical review*, 71(9):622, 1947.

[17] MS Dresselhaus, G Dresselhaus, and Riichiro Saito. Carbon fibers based on c 60 and their symmetry. *Physical Review B*, 45(11):6234, 1992.

[18] K. S. Novoselov, A. K. Geim, S. V. Morozov, D. Jiang, Y. Zhang, S. V. Dubonos, I. V. Grigorieva, and A. A. Firsov. Electric field effect in atomically thin carbon films. *Science*, 306(5696):666–669, 2004.

[19] Xuesong Li, Weiwei Cai, Jinho An, Seyoung Kim, Junghyo Nah, Dongxing Yang, Richard Piner, Aruna Velamakanni, Inhwa Jung, Emanuel Tutuc, et al. Large-area synthesis of high-quality and uniform graphene films on copper foils. *science*, 324(5932):1312–1314, 2009.

[20] Ibrahim Fakih, Oliver Durnan, Farzaneh Mahvash, Ilargi Napal, Alba Centeno, Amaia Zurutuza, Viviane Yargeau, and Thomas Szkopek. Selective ion sensing with high resolution large area graphene field effect transistor arrays. *Nature Communications*, accepted for publication.

[21] Altynay Kaidarova, Mohammed Asadullah Khan, Marco Marengo, Liam Swanepoel, Alexander Przybysz, Cobus Muller, Andreas Fahlman, Ulrich Buttner, Nathan R Geraldi, Rory P Wilson, et al. Wearable multifunctional printed graphene sensors. *npj Flexible Electronics*, 3(1):1–10, 2019.

[22] Brian T Schaefer, Lei Wang, Alexander Jarjour, Kenji Watanabe, Takashi Taniguchi, Paul L McEuen, and Katja C Nowack. Magnetic field detection limits for ultraclean graphene hall sensors. *Nature communications*, 11(1):1–8, 2020.

[23] AA Kaverzin, A Shytov Mayorov, A Shytov, and DW Horsell. Impurities as a source of 1/f noise in graphene. *Physical Review B*, 85(7):075435, 2012.

[24] Maxim A Stolyarov, Guanxiong Liu, Sergey L Rumyantsev, Michael Shur, and Alexander A Balandin. Suppression of 1/f noise in near-ballistic h-BN-graphene-h-BN heterostructure field-effect transistors. *Applied Physics Letters*, 107(2):023106, 2015.

[25] Chandan Kumar and Anindya Das. Effect of boron nitride defects and charge inhomogeneity on 1/f noise in encapsulated graphene. *Applied physics letters*, 119(22), 2021.

[26] Adil Rehman, Juan Antonio Delgado Notario, Juan Salvador Sanchez, Yahya Moubarak Meziani, Grzegorz Cywiński, Wojciech Knap, Alexander A Balandin, Michael Levinshtein, and Sergey Rumyantsev. Nature of the 1/f noise in graphene—direct evidence for the mobility fluctuation mechanism. *Nanoscale*, 14(19):7242–7249, 2022.

[27] Masahiro Kamada, Antti Laitinen, Weijun Zeng, Marco Will, Jayanta Sarkar, Kirsi Tappura, Heikki Seppa, and Pertti Hakonen. Electrical low-frequency 1/f γ noise due to surface diffusion of scatterers on an ultra-low-noise graphene platform. *Nano Letters*, 21(18):7637–7643, 2021.

[28] Gunter Dörfel. The early history of thermal noise: The long way to paradigm change. *Annalen der Physik*, 524(8):117–121, 2012.

[29] Rep Kubo. The fluctuation-dissipation theorem. *Reports on progress in physics*, 29(1):255, 1966.

[30] Lev Davidovich Landau, Evgenij Mihajlovič Lifšic, Evgenii Mikhailovich Lifshitz, and LP Pitaevskii. *Statistical physics: theory of the condensed state*, volume 9. Butterworth-Heinemann, 1980.

[31] Ngoc Anh Minh Tran, Aditya Savitha Dutt, Nithin Bharadwaj Pulumati, Heiko Reith, Anjun Hu, Alexandre Dumont, Kornelius Nielsch, A-MS Tremblay, Gabi Schierning, Bertrand Reulet, et al. Fluctuation-dissipation in thermoelectric sensors. *Europhysics Letters*, 141(2):26002, 2023.

[32] John B Johnson. The schottky effect in low frequency circuits. *Physical review*, 26(1):71, 1925.

[33] FN Hooge. The relation between 1/f noise and number of electrons. *Physica B: Condensed Matter*, 162(3):344–352, 1990.

[34] R. F. Voss. 1/f noise and fractals in economic time series. In José L. Encarnação, Georgios Sakas, Heinz-Otto Peitgen, and Gabriele Englert, editors, *Fractal Geometry and Computer Graphics*, pages 45–52, Berlin, Heidelberg, 1992. Springer Berlin Heidelberg.

[35] David L Gilden, Thomas Thornton, and Mark W Mallon. 1/f noise in human cognition. *Science*, 267(5205):1837–1839, 1995.

[36] Alexander A. Balandin. Low-frequency 1/f noise in graphene devices. *Nature Nanotechnology*, 8(8):549–555, Aug 2013.

[37] Daniel Bauza and Naima Guenifi. Study of si (100)-sio2 interface trap time constant distributions in large area conventional mosfets-comparison with submicron devices. *ECS Transactions*, 97(1):83, 2020.

[38] Ngoc Anh Minh Tran, Ibrahim Fakih, Oliver Durnan, Anjun Hu, Ayse Melis Aygar, Ilargi Napal, Alba Centeno, Amaia Zurutuza, Bertrand Reulet, and Thomas Szkopek. Graphene field effect transistor scaling for ultra-low-noise sensors. *Nanotechnology*, 32(4):045502, 2020.

[39] Maurice Bertram Priestley. *Spectral analysis and time series: probability and mathematical statistics*. Academic Press, San Diego, 1981.

[40] T Chan Carusone, D Johns, and K Martin. Analog integrated circuit design. *New York: Wiley. Hannane Gholamnataj was born in Babolsar, Iran, on September*, 16:1984, 2012.

[41] Art Kay. *Operational amplifier noise: techniques and tips for analyzing and reducing noise*. Elsevier, 2012.

[42] Gastón A Crespo. Recent advances in ion-selective membrane electrodes for in situ environmental water analysis. *Electrochimica Acta*, 245:1023–1034, 2017.

[43] Lane A Baker. Perspective and prospectus on single-entity electrochemistry. *Journal of the American Chemical Society*, 140(46):15549–15559, 2018.

[44] Yevedzo E Chipangura, Brian D Spindler, Philippe Bühlmann, and Andreas Stein. Design criteria for nanostructured carbon materials as solid contacts for ion-selective sensors. *Advanced Materials*, 36(8):2309778, 2024.

[45] Ferenc Szabadvary and Ralph E Oesper. Development of the ph concept: A historical survey. *Journal of Chemical Education*, 41(2):105, 1964.

[46] The absolute electrode potential: an explanatory note (recommendations 1986). *Journal of Electroanalytical Chemistry and Interfacial Electrochemistry*, 209(2):417–428, 1986.

[47] Donald T Sawyer, Andrzej Sobkowiak, and Julian L Roberts. Electrochemistry for chemists. page 192, 1995.

[48] Robert B Fischer. Ion-selective electrodes, 1974.

[49] S. Głab, M. Maj-Żurawska, and A. Hulanicki. Ion-selective electrodes — glass electrodes. In *Reference Module in Chemistry, Molecular Sciences and Chemical Engineering*. Elsevier, 2013.

[50] Justin M Zook, Jan Langmaier, and Ernő Lindner. Current-polarized ion-selective membranes: The influence of plasticizer and lipophilic background electrolyte on

concentration profiles, resistance, and voltage transients. *Sensors and Actuators B: Chemical*, 136(2):410–418, 2009.

[51] Piet Bergveld. Development of an ion-sensitive solid-state device for neurophysiological measurements. *IEEE Transactions on Biomedical Engineering*, (1):70–71, 1970.

[52] Nicole Rusk. Torrents of sequence. *Nature Methods*, 8(1):44–44, 2011.

[53] Denis J Murphy. Using modern plant breeding to improve the nutritional and technological qualities of oil crops. *OCL*, 21(6):D607, 2014.

[54] Piet Bergveld. Thirty years of isfetology: What happened in the past 30 years and what may happen in the next 30 years. *Sensors and Actuators B: Chemical*, 88(1):1–20, 2003.

[55] Ibrahim Fakih, Farzaneh Mahvash, Mohamed Siaj, and Thomas Szkopek. Sensitive precise pH measurement with large-area graphene field-effect transistors at the quantum-capacitance limit. *Phys. Rev. Applied*, 8:044022, Oct 2017.

[56] B Lubbers and Andreas Schober. Comparing the isfet to the glass electrode: advantages, challenges and similarities. *Chemia Analityczna*, 54(6):1121–1148, 2009.

[57] Jonathan M Rothberg, Wolfgang Hinz, Todd M Rearick, Jonathan Schultz, William Mileski, Mel Davey, John H Leamon, Kim Johnson, Mark J Milgrew, Matthew

Edwards, et al. An integrated semiconductor device enabling non-optical genome sequencing. *Nature*, 475(7356):348–352, 2011.

[58] Timothy S Duffy, Derek M Hall, and Serguei N Lvov. Increasing the lifespan of reference electrodes by increasing the diffusion length. *Electrochimica Acta*, 438:141562, 2023.

[59] Evan L Anderson, Blair K Troudt, and Philippe Buhlmann. Easy-to-make capillary-based reference electrodes with controlled, pressure-driven electrolyte flow. *ACS sensors*, 6(6):2211–2217, 2021.

[60] John Bertrand Johnson. Thermal agitation of electricity in conductors. *Physical review*, 32(1):97, 1928.

[61] Neil W Ashcroft, N David Mermin, et al. *Solid state physics*, volume 2005. Holt, Rinehart and Winston, New York, 1976.

[62] David M. Rowe. *CRC Handbook of Thermoelectrics*. CRC Press, Boca Raton, 1995.

[63] Christophe Goupil, Wolfgang Seifert, Knud Zabrocki, Eckhart Müller, and G. Jeffrey Snyder. Thermodynamics of thermoelectric phenomena and applications. *Entropy*, 13(8):1481–1517, 2011.

[64] Guodong Li, Javier Garcia Fernandez, David Alberto Lara Ramos, Vida Barati, Nicolás Pérez, Ivan Soldatov, Heiko Reith, Gabi Schierning, and Kornelius Nielsch. Integrated

microthermoelectric coolers with rapid response time and high device reliability. *Nature Electronics*, 1(10):555–561, 2018.

[65] Raj K. Pathria. *Statistical Mechanics*. Butterworth-Heineman, Oxford, 1996.

[66] Lev D. Landau and Evgeny M. Lifshitz. *Course of Theoretical Physics: Statistical Physics Part 1*. Elsevier, 1981.

[67] Supplemental material is available, including theoretical analysis of electric field and temperature gradient fluctuations, voltage fluctuation measurement of a thin film resistor, voltage fluctuation measurement of a N=105 thermoelectric micro-device, numerical model fits of voltage fluctuation and impedance spectra, Seebeck coefficient measurements.

[68] Theodore C. Harman. Special techniques for measurement of thermoelectric properties. *Journal of Applied Physics*, 29(9):1373–1374, 1958.

[69] Adam D Downey, Timothy P Hogan, and Bruce Cook. Characterization of thermoelectric elements and devices by impedance spectroscopy. *Review of Scientific Instruments*, 78(9):093904, 2007.

[70] Jorge García-Cañadas and Gao Min. Impedance spectroscopy models for the complete characterization of thermoelectric materials. *Journal of Applied Physics*, 116(17):174510, 2014.

[71] Jorge García-Cañadas and Gao Min. Thermal dynamics of thermoelectric phenomena from frequency resolved methods. *AIP Advances*, 6(3):035008, 2016.

[72] Yasuhiro Hasegawa, Ryoei Homma, and Mioko Ohtsuka. Thermoelectric module performance estimation based on impedance spectroscopy. *Journal of Electronic Materials*, 45(3):1886–1893, 2016.

[73] Wenjuan Tian, Cangling Wang, Jianqing Wang, Qiuhua Chen, Jianfei Sun, Can Li, Xing Wang, and Ning Gu. A high precision apparatus for intracellular thermal response at single-cell level. *Nanotechnology*, 26(35):355501, 2015.

[74] Fredrik Schedin, Andrei Konstantinovich Geim, Sergei Vladimirovich Morozov, EW Hill, Peter Blake, MI Katsnelson, and Kostya Sergeevich Novoselov. Detection of individual gas molecules adsorbed on graphene. *Nature Materials*, 6(9):652–655, 2007.

[75] J-H Chen, Ci Jang, Shaffique Adam, MS Fuhrer, Ellen D Williams, and Masa Ishigami. Charged-impurity scattering in graphene. *Nature Physics*, 4(5):377–381, 2008.

[76] Wangyang Fu, Cornelia Nef, Oren Knopfmacher, Alexey Tarasov, Markus Weiss, Michel Calame, and Christian Schönenberger. Graphene transistors are insensitive to pH changes in solution. *Nano Letters*, 11(9):3597–3600, 2011.

[77] Ning Gao, Teng Gao, Xiao Yang, Xiaochuan Dai, Wei Zhou, Anqi Zhang, and Charles M. Lieber. Specific detection of biomolecules in physiological solutions using

graphene transistor biosensors. *Proceedings of the National Academy of Sciences*, 113(51):14633–14638, 2016.

[78] Pierre L Levesque, Shadi S Sabri, Carla M Aguirre, Jonathan Guillemette, Mohamed Siaj, Patrick Desjardins, Thomas Szkopek, and Richard Martel. Probing charge transfer at surfaces using graphene transistors. *Nano Letters*, 11(1):132–137, 2011.

[79] Ibrahim Fakih, Shadi Sabri, Farzaneh Mahvash, Matthieu Nannini, Mohamed Siaj, and Thomas Szkopek. Large area graphene ion sensitive field effect transistors with tantalum pentoxide sensing layers for pH measurement at the nernstian limit. *Applied Physics Letters*, 105(8):083101, 2014.

[80] Hongmei Li, Yihao Zhu, Md Sayful Islam, Md Anisur Rahman, Kenneth B Walsh, and Goutam Koley. Graphene field effect transistors for highly sensitive and selective detection of K+ ions. *Sensors and Actuators B: Chemical*, 253:759–765, 2017.

[81] Ibrahim Fakih, Alba Centeno, Amaia Zurutuza, Boutheina Ghaddab, Mohamed Siaj, and Thomas Szkopek. High resolution potassium sensing with large-area graphene field-effect transistors. *Sensors and Actuators B: Chemical*, 291:89–95, 2019.

[82] Cao Thi Thanh, Nguyen Hai Binh, Nguyen [Van Tu], Vu Thi Thu, Maxime Bayle, Matthieu Paillet, Jean Louis Sauvajol, Phan Bach Thang, Tran Dai Lam, Phan Ngoc Minh, and Nguyen [Van Chuc]. An interdigitated ISFET-type sensor based on LPCVD

grown graphene for ultrasensitive detection of carbaryl. *Sensors and Actuators B: Chemical*, 260:78 – 85, 2018.

[83] Xiaochen Dong, Yumeng Shi, Wei Huang, Peng Chen, and Lain-Jong Li. Electrical detection of DNA hybridization with single-base specificity using transistors based on CVD-grown graphene sheets. *Advanced Materials*, 22(14):1649–1653, 2010.

[84] Yasuhide Ohno, Shogo Okamoto, Kenzo Maehashi, and Kazuhiko Matsumoto. Direct electrical detection of DNA hybridization based on electrolyte-gated graphene field-effect transistor. *Japanese Journal of Applied Physics*, 52(11R):110107, nov 2013.

[85] Guangyu Xu, Jeffrey Abbott, Ling Qin, Kitty YM Yeung, Yi Song, Hosang Yoon, Jing Kong, and Donhee Ham. Electrophoretic and field-effect graphene for all-electrical DNA array technology. *Nature Communications*, 5(1):1–9, 2014.

[86] Shicai Xu, Jian Zhan, Baoyuan Man, Shouzhen Jiang, Weiwei Yue, Shoubao Gao, Chengang Guo, Hanping Liu, Zhenhua Li, Jihua Wang, et al. Real-time reliable determination of binding kinetics of DNA hybridization using a multi-channel graphene biosensor. *Nature Communications*, 8:14902, 2017.

[87] Wangyang Fu, Lingyan Feng, Gregory Panaitov, Dmitry Kireev, Dirk Mayer, Andreas Offenhäusser, and Hans-Joachim Krause. Biosensing near the neutrality point of graphene. *Science Advances*, 3(10):e1701247, 2017.

[88] Yasuhide Ohno, Kenzo Maehashi, and Kazuhiko Matsumoto. Label-free biosensors based on aptamer-modified graphene field-effect transistors. *Journal of the American Chemical Society*, 132(51):18012–18013, 2010.

[89] Shogo Okamoto, Yasuhide Ohno, Kenzo Maehashi, Koichi Inoue, and Kazuhiko Matsumoto. Immunosensors based on graphene field-effect transistors fabricated using antigen-binding fragment. *Japanese Journal of Applied Physics*, 51(6S):06FD08, 2012.

[90] Grant Saltzgaber, Peter M Wojcik, Tal Sharf, Matthew R Leyden, Jenna L Wardini, Christopher A Heist, Adeniyi A Adenuga, Vincent T Remcho, and Ethan D Minot. Scalable graphene field-effect sensors for specific protein detection. *Nanotechnology*, 24(35):355502, aug 2013.

[91] Mitchell B Lerner, Felipe Matsunaga, Gang Hee Han, Sung Ju Hong, Jin Xi, Alexander Crook, Jose Manuel Perez-Aguilar, Yung Woo Park, Jeffery G Saven, Renyu Liu, et al. Scalable production of highly sensitive nanosensors based on graphene functionalized with a designed G protein-coupled receptor. *Nano Letters*, 14(5):2709–2714, 2014.

[92] Zhuang Hao, Yibo Zhu, Xuejun Wang, Pavana G Rotti, Christopher DiMarco, Scott R Tyler, Xuezeng Zhao, John F Engelhardt, James Hone, and Qiao Lin. Real-time monitoring of insulin using a graphene field-effect transistor aptameric nanosensor. *ACS Applied Materials & Interfaces*, 9(33):27504–27511, 2017.

[93] Nesha M. Andoy, Marcin S. Filipiak, Daniel Vetter, Óscar Gutiérrez-Sanz, and Alexey Tarasov. Graphene-based electronic immunosensor with femtomolar detection limit in whole serum. *Advanced Materials Technologies*, 3(12):1800186, 2018.

[94] J. Inczédy, T. Lengyel, A.M. Ure, A. Gelencsér, International Union of Pure, and Applied Chemistry. *Compendium of Analytical Nomenclature: Definitive Rules 1997*. IUPAC Chemical Data Series. Blackwell Science, 1998.

[95] Atindra Nath Pal, Ageeth A Bol, and Arindam Ghosh. Large low-frequency resistance noise in chemical vapor deposited graphene. *Applied Physics Letters*, 97(13):133504, 2010.

[96] Guangyu Xu, Carlos M Torres Jr, Yuegang Zhang, Fei Liu, Emil B Song, Minsheng Wang, Yi Zhou, Caifu Zeng, and Kang L Wang. Effect of spatial charge inhomogeneity on 1/f noise behavior in graphene. *Nano Letters*, 10(9):3312–3317, 2010.

[97] Yan Zhang, Emilio E Mendez, and Xu Du. Mobility-dependent low-frequency noise in graphene field-effect transistors. *ACS nano*, 5(10):8124–8130, 2011.

[98] Paritosh Karnatak, Twarakavi Sai, Srijit Goswami, Subhamoy Ghatak, Sanjeev Kaushal, and Arindam Ghosh. Current crowding mediated large contact noise in graphene field-effect transistors. *Nature Communications*, 7:13703, 12 2016.

[99] Friits N Hooge. 1/f noise sources. *IEEE Transactions on Electron Devices*, 41(11):1926–1935, 1994.

[100] J Liu, X Wu, Z Zhang, S Wakida, and K Higashi. Sulfate ion-selective field effect transistors prepared by sol–gel technique. *Sensors and Actuators B: Chemical*, 66(1-3):216–218, 2000.

[101] Sheng-Ren Chang and Hsin Chen. A CMOS-compatible, low-noise ISFET based on high efficiency ion-modulated lateral-bipolar conduction. *Sensors*, 9(10):8336–8348, 2009.

[102] Jayeeta Basu and Chirasree RoyChaudhuri. Graphene nanogrids FET immunosensor: signal to noise ratio enhancement. *Sensors*, 16(10):1481, 2016.

[103] Sameer Grover, Sudipta Dubey, John P Mathew, and Mandar M Deshmukh. Limits on the bolometric response of graphene due to flicker noise. *Applied Physics Letters*, 106(5):051113, 2015.

[104] Zengguang Cheng, Qiang Li, Zhongjun Li, Qiaoyu Zhou, and Ying Fang. Suspended graphene sensors with improved signal and reduced noise. *Nano Letters*, 10(5):1864–1868, 2010.

[105] Chandan Kumar, Manabendra Kuiri, Jeil Jung, Tanmoy Das, and Anindya Das. Tunability of 1/f noise at multiple dirac cones in hBN encapsulated graphene devices. *Nano Letters*, 16(2):1042–1049, 2016.

[106] Heather N Arnold, Vinod K Sangwan, Scott W Schmucker, Cory D Cress, Kyle A Luck, Adam L Friedman, Jeremy T Robinson, Tobin J Marks, and Mark C Hersam. Reducing flicker noise in chemical vapor deposition graphene field-effect transistors. *Applied Physics Letters*, 108(7):073108, 2016.

[107] Brice Grandchamp, Sebastien Fregonese, Cédric Majek, Cyril Hainaut, Cristell Maneux, Nan Meng, Henri Happy, and Thomas Zimmer. Characterization and modeling of graphene transistor low-frequency noise. *IEEE transactions on Electron Devices*, 59(2):516–519, 2011.

[108] Nikolaos Mavredakis, Ramon Garcia Cortadella, Andrea Bonaccini Calia, Jose A Garrido, and David Jiménez. Understanding the bias dependence of low frequency noise in single layer graphene FETs. *Nanoscale*, 10(31):14947–14956, 2018.

[109] Xuefei Li, Xiaobo Lu, Tiaoyang Li, Wei Yang, Jianming Fang, Guangyu Zhang, and Yanqing Wu. Noise in graphene superlattices grown on hexagonal boron nitride. *ACS Nano*, 9(11):11382–11388, 2015.

[110] Vidya Kochat, Anindita Sahoo, Atindra Nath Pal, Sneha Eashwer, Gopalakrishnan Ramalingam, Arjun Sampathkumar, Ryugu Tero, Tran Viet Thu, Sanjeev Kaushal,

Hiroshi Okada, et al. Origin of 1/f noise in graphene produced for large-scale applications in electronics. *IET Circuits, Devices & Systems*, 9(1):52–58, 2015.

[111] Sukang Bae, Hyeongkeun Kim, Youngbin Lee, Xiangfan Xu, Jae-Sung Park, Yi Zheng, Jayakumar Balakrishnan, Tian Lei, Hye Ri Kim, Young Il Song, et al. Roll-to-roll production of 30-inch graphene films for transparent electrodes. *Nature Nanotechnology*, 5(8):574, 2010.

[112] Libo Gao, Wencai Ren, Huilong Xu, Li Jin, Zhenxing Wang, Teng Ma, Lai-Peng Ma, Zhiyong Zhang, Qiang Fu, Lian-Mao Peng, et al. Repeated growth and bubbling transfer of graphene with millimetre-size single-crystal grains using platinum. *Nature Communications*, 3(1):1–7, 2012.

[113] Abhay Shivayogimath, Patrick Rebsdorf Whelan, David MA Mackenzie, Birong Luo, Deping Huang, Da Luo, Meihui Wang, Lene Gammelgaard, Haofei Shi, Rodney S Ruoff, et al. Do-it-yourself transfer of large-area graphene using an office laminator and water. *Chemistry of Materials*, 31(7):2328–2336, 2019.

[114] G. E. Moore. Cramming more components onto integrated circuits. *Electronics*, 38(8):666–669, 1965.

[115] Andrzej Lewenstam, Bartosz Bartoszewicz, Jan Migdalski, and Adam Kochan. Solid contact reference electrode with a pvc-based composite electroactive element fabricated by 3d printing. *Electrochemistry Communications*, 109:106613, 2019.

[116] Beth E Murdock, Craig G Armstrong, Daniel E Smith, Nuria Tapia-Ruiz, and Kathryn E Toghill. Misreported non-aqueous reference potentials: the battery research endemic. *Joule*, 6(5):928–934, 2022.

[117] Luigi Fabbrizzi. The ferrocenium/ferrocene couple: a versatile redox switch. *ChemTexts*, 6:1–20, 2020.

[118] Avishek Paul, Raffaele Borrelli, Houssny Bouyanfif, Sébastien Gottis, and Frédéric Sauvage. Tunable redox potential, optical properties, and enhanced stability of modified ferrocene-based complexes. *ACS omega*, 4(12):14780–14789, 2019.

[119] Christian Spånslätt, Florian Stäbler, Eugene V Sukhorukov, and Janine Splettstoesser. Impact of potential and temperature fluctuations on charge and heat transport in quantum hall edges in the heat coulomb blockade regime. *arXiv preprint arXiv:2406.08910*, 2024.

[120] Roland Weiss, Roland Mattheis, and Günter Reiss. Advanced giant magnetoresistance technology for measurement applications. *Measurement Science and Technology*, 24(8):082001, 2013.

[121] Bruno Pellegrini. 1/f noise in graphene. *The European Physical Journal B*, 86:1–12, 2013.

[122] Vilius Palenskis, Justinas Glemža, Juozas Vyšniauskas, and Jonas Matukas. Carrier density and mobility fluctuations due to carrier retrapping process in homogeneous semiconductors. In *2017 International Conference on Noise and Fluctuations (ICNF)*, pages 1–4. IEEE, 2017.

[123] Masahiro Kamada, Weijun Zeng, Antti Laitinen, Jayanta Sarkar, Sheng-Shiuan Yeh, Kirsi Tappura, Heikki Seppä, and Pertti Hakonen. Suppression of 1/f noise in graphene due to anisotropic mobility fluctuations induced by impurity motion. *Communications Physics*, 6(1):207, 2023.

[124] Jincan Zhang, Luzhao Sun, Kaicheng Jia, Xiaoting Liu, Ting Cheng, Hailin Peng, Li Lin, and Zhongfan Liu. New growth frontier: Superclean graphene. *ACS nano*, 14(9):10796–10803, 2020.

[125] Na Xin, James Lourembam, Piranavan Kumaravadivel, AE Kazantsev, Zefei Wu, Ciaran Mullan, Julien Barrier, Alexandra A Geim, IV Grigorieva, Artem Mishchenko, et al. Giant magnetoresistance of dirac plasma in high-mobility graphene. *Nature*, 616(7956):270–274, 2023.

[126] Yongjun Tan. Sensing localised corrosion by means of electrochemical noise detection and analysis. *Sensors and Actuators B: Chemical*, 139(2):688–698, 2009.

[127] Zhongwu Li, Rahul Prasanna Misra, Yuhao Li, Yun-Chiao Yao, Sidi Zhao, Yuliang Zhang, Yunfei Chen, Daniel Blankschtein, and Aleksandr Noy. Breakdown of the

nernst–einstein relation in carbon nanotube porins. *Nature Nanotechnology*, 18(2):177–183, 2023.

[128] Enno Katelhon, Kay J Krause, Klaus Mathwig, Serge G Lemay, and Bernhard Wolfrum. Noise phenomena caused by reversible adsorption in nanoscale electrochemical devices. *ACS nano*, 8(5):4924–4930, 2014.